Pure Appl. Chem., Vol. 82, No. 11, pp. 2027–2053, 2010.
doi:10.1351/PAC-CON-09-09-18

Vapor-phase synthesis of one-dimensional ZnS, CdS, and $Zn_xCd_{1-x}S$ nanostructures*

Tianyou Zhai‡, Xiaosheng Fang‡, Haibo Zeng, Xijin Xu‡, Yoshio Bando, and Dmitri Golberg

International Center for Young Scientists (ICYS) and International Center for Materials Nanoarchitectonics (MANA), National Institute for Materials Science (NIMS), Namiki 1-1, Tsukuba, Ibaraki 305-0044, Japan

Abstract: One-dimensional (1D) nanostructures have received prime attention due to their high potential in understanding fundamental physical concepts and constructing nanoscale electronic devices. ZnS and CdS, the well-known direct and wide bandgap semiconductors, have recently attracted significant research interest due to their special properties and applications in sensing, optoelectronics, piezoelectronics, and lasing. This article reviews the most recent activities in ZnS and CdS nanostructures, with an emphasis on the authors' own results, and on 1D ZnS and CdS nanostructures, especially those synthesized using vapor deposition techniques. The review begins with a survey of ZnS and CdS nanostructures, and then is primarily focused on their 1D nanostructures, syntheses, characterizations, formation mechanisms, and optical and field-emission (FE) properties. Additionally, developments of $Zn_xCd_{1-x}S$ composite nanostructures, including nanocombs and zigzag nanowires, are also discussed. Finally, we conclude this review with the perspectives and outlook on the future developments in this field.

Keywords: CdS; nanomaterials; nanostructures; vapor-phase synthesis; ZnS.

INTRODUCTION

One-dimensional (1D) nanostructures such as nanowires, nanobelts, nanotubes, and nanorods have stimulated an increasing interest due to their importance in basic scientific research and potential technological applications [1–3]. It is generally accepted that 1D nanostructures are ideal systems for exploring a large number of novel phenomena at the nanoscale and investigating the size and dimensionality dependence of functional properties [4]. They are also expected to play important roles as both interconnects and the key units in fabricating electronic, optoelectronic, electrochemical, and electromechanical devices with nanoscale dimensions [5]. As important II–VI semiconductors, ZnS and CdS are some of the first semiconductors discovered and probably some of the most important electronic and optoelectronic materials with prominent applications in nonlinear optical devices, flat panel displays, light-emitting diodes, laser, logic gates, transistors, etc. [6,7].

It is evident that the research on 1D ZnO nanostructures has rapidly expanded in recent years because of their special structures and novel properties. As pointed out by Zhong Lin Wang in one of the latest reviews, 1D ZnO has been one of the few dominant nanomaterials in nanotechnology along with

*Paper based on a presentation at the 5th International Symposium on Novel Materials and Their Synthesis (NMS-V) and the 19th International Symposium on Fine Chemistry and Functional Polymers (FCFP-XIX), 18–22 October 2009, Shanghai, China. Other presentations are published in this issue, pp. 1975–2229.

‡Corresponding authors: E-mail: zhai.tianyou@gmail.com or zhai.tianyou@nims.go.jp (T. Y. Zhai), fang.xiaosheng@nims.go.jp (X. S. Fang), xu.xijin@nims.go.jp (X. J. Xu); Fax: 81-29-851-6280

carbon nanotubes (CNTs) and silicon nanowires. The number of publications and the cross-referenced areas based on ZnO nanostructures are as large and as important as the literatures in quantum computing, CNTs, semiconductor thin films, and dark matter [8,9]. This comment is also evidenced by the data from Fig. 1, the number of published papers related to nano-ZnO has rapidly expanded since 2000. From Table 1, one can easily see that ZnS and CdS have similar fundamental physical properties with ZnO, including crystal structures, lattice constants, and so on. Thus, the interesting nanoscale morphologies and novel properties of nanoscale ZnS and CdS could rival those of ZnO. In fact, the research on 1D ZnS and CdS nanostructures has recently come to the forefront owing to their potential merits for understanding fundamental physical concepts and for the utilization in nanoscale optoelectronic devices [10]. Although the number of publications related to nanoscale ZnS and CdS is smaller than that for ZnO (Fig. 1), these numbers are notably increasing in recent years, especially with respect to the 1D ZnS and CdS nanostructure-oriented papers.

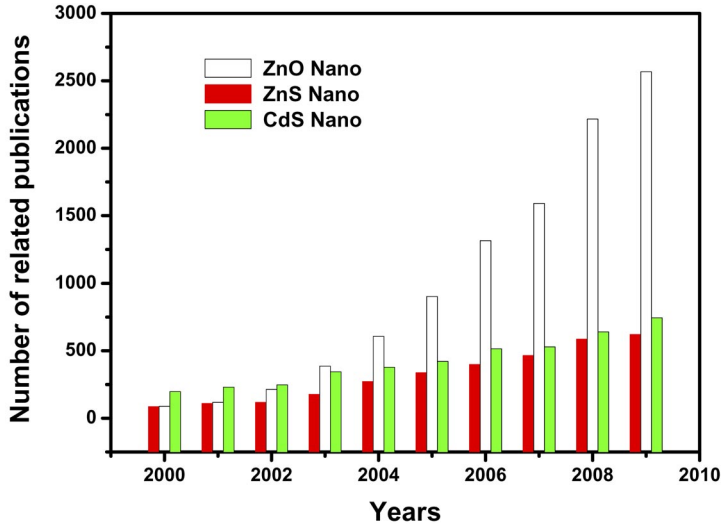

Fig. 1 A plot illustrating the number of published papers related to nano*- ZnO, ZnS, or CdS each year since 2000 (Web of Science).

Table 1 Comparison of some fundamental ZnO, ZnS, and CdS physical properties [11].

	Crystal structures	Lattice constants		Bandgap (eV)	Exciton binding energy (meV)	Work function (eV)	Melting point (K)
		a (nm)	*c* (nm)				
ZnO	Hexagonal	0.3249	0.5207	3.37	60	5.3	2248
ZnS	Hexagonal	0.3823	0.6261	3.77	39	7.0	2103
	Cubic	0.5410	—	3.72			1800
CdS	Hexagonal	0.3820	0.6257	2.52	29.4	4.2	2023
	Cubic	0.5811	—				—

This article reviews the most recent research activities in ZnS and CdS nanostructures, with an emphasis on the authors' own results, and on 1D ZnS and CdS nanostructures, especially on those synthesized using vapor depositions.

CRYSTALLOGRAPHIC STRUCTURE OF ZnS AND CdS

Both ZnS and CdS have two kinds of structures, namely, zinc blend crystal structures and wurtzite structures. The zinc blend and wurtzite structures are cubic and hexagonal, respectively, and these two structures are very similar [12]. As shown in Fig. 2, the stacking sequence of the close-packed planes of zinc blende [the (111) planes] is represented by the ABCABCABC repeating pattern, while that of wurtzite is represented by the ABABAB repeating pattern. Wurtzite ZnS (or CdS) can be described as a number of alternating planes composed of tetrahedral coordinated S^{2-} and Zn^{2+} (or Cd^{2+}) ions, stacked along the *c*-axis.

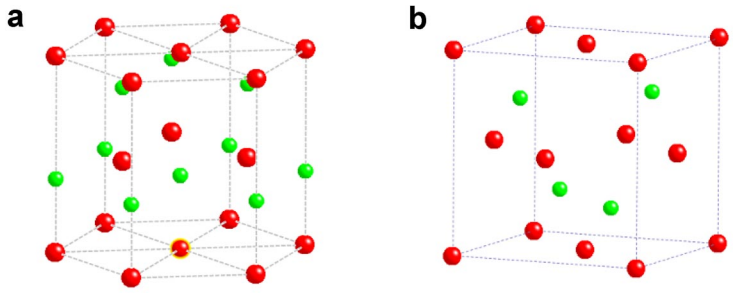

Fig. 2 Two kinds of structures in ZnS and CdS: (a) hexagonal (wurtzite) crystal structure; (b) cubic (zinc blende) structure. Red and green balls represent Zn or Cd, and S, respectively.

Another important characteristic of ZnS and CdS is the polar surfaces. The most common polar surface is the basal plane. The oppositely charged ions produce positively charged Zn, Cd-(0001) and S-(000-1) polar surfaces, resulting in a normal dipole moment and spontaneous polarization along the *c*-axis, as well as in divergence in surface energy. Wurtzite ZnS and CdS possess anisotropic growth for two reasons. One is that different crystallographic planes have different surface energies, and another one is that their surface polarity and chemical activities differ [13].

SYNTHESIS ROUTES TOWARD 1D NANOSTRUCTURES AND NANOMATERIALS

During the past decade, many methodologies have been developed to synthesize 1D nanostructures and nanomaterials. Overall, they can be categorized into two major approaches based on the reaction media that are used during the preparation: solution- and vapor-phase-based processes [14]. Solution-based approaches mainly include solvothermal chemical synthesis [15–18], template-directed synthesis [19–21], solution–liquid–solid method [22], sol-gel technique [23], self-assembly method [24], and electrospinning method [25,26]. These growth methods provide more flexible synthetic process and a relatively low cost. Keeping in mind a few exciting reviews related to the solution-based methods [27–29], we skip these techniques herein and solely focus on the vapor-phase synthesis.

Vapor-phase methods are the kinds of approaches in which a crystal is grown by depositing the material directly from a vapor or a gaseous state. It is probably the most extensively explored approach forming 1D nanostructures. In principle, it is possible to process any solid material into 1D nanostructures by controlling the synthesis conditions. Several techniques can be assigned to vapor-phase methods, such as thermal evaporation, chemical vapor deposition (CVD), and metal-organic chemical

vapor deposition (MOCVD) [30]. Among them, thermal evaporation is one of the simplest and most popular methods. The basic process relies on sublimation of source materials in a powder form at a high temperature, and subsequent vapor deposition at a certain temperature to form desired nanostructures. A typical experimental system is shown in Fig. 3. The synthesis is performed in an alumina or quartz tube, which is placed in a horizontal tube furnace. High-purity powders put in an alumina (or quartz, graphite) boat are loaded in the middle of the furnace, i.e., its highest temperature region. The substrates for collecting the desired nanostructures are usually placed down-stream of a carrier gas. The substrates can be silicon wafers, sapphire plates, or porous anodic alumina (PAA) templates. Both ends of the tube are covered by stainless steel caps and sealed with O-rings. Cooling water flows inside the cover caps to achieve a reasonable temperature gradient in the tube. The furnace pressure can be controlled by the pumping speed. Recently, our group developed a new vapor-phase synthesis apparatus based on a vertical induction furnace, as shown in Fig. 4. The furnace consists of a fused quartz tube and an induc-

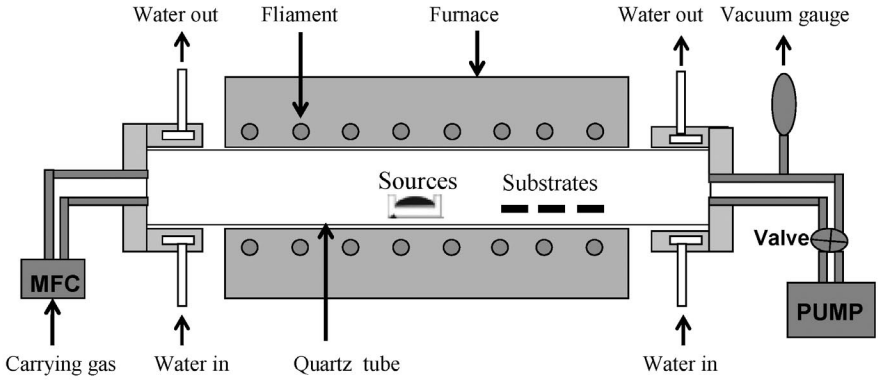

Fig. 3 Schematic diagram of a horizontal furnace for the vapor-phase growth.

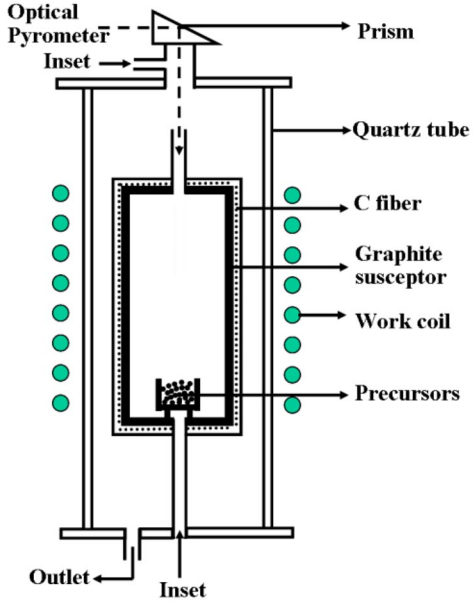

Fig. 4 Schematic diagram of a vertical induction furnace for the vapor-phase growth.

tion-heating cylinder made of high-purity graphite coated with a graphite fiber thermo-insulating layer. The length, width, and inner structure of an induction heating cylinder can be changed for different experiments. The system has inlet and outlet graphite pipes for the introduction of reactive and carrier gases. The chemical reactions take place during the synthesis process, this technique is referred to as CVD. If precursors contain metallo-organics the approach becomes MOCVD. In our experiments, both horizontal and vertical induction furnaces have been used, and all techniques, including thermal evaporation, CVD, and MOCVD, have been utilized to synthesize 1D nanostructures in different materials' systems.

SYNTHESIS, CHARACTERIZATION AND PROPERTIES OF 1D ZnS, CdS, AND $Zn_xCd_{1-x}S$ NANOSTRUCTURES

ZnS 1D nanostructures

Recently, various 1D ZnS nanostructures have been fabricated. For example, ZnS nanowires were synthesized via an MOCVD process using a single-source molecular precursor [31], thermal evaporation with the presence of a Au catalyst [32,33], a templating route by γ-irradiation [34], intermittent laser ablation-catalytic growth [35], pulsed laser vaporization (PLV) [36], electrochemical deposition [37], hydrogen-assisted thermal evaporation [38], etc. ZnS nanotubes were fabricated using a high-temperature thermal-chemical reaction route [39], chemical conversion of ZnO columns [40], a thermochemial method [41], a solution route using CNTs as the templates [42], an MOCVD-template method [43], etc. ZnS nanobelts or nanoribbons were prepared by means of a thermal evaporation process [44–46], a hydrogen-assisted thermal evaporation synthesis [47], a PLV method [48], CVD [49], etc. ZnS tetrarods were fabricated by thermal evaporation of a ZnS and SiO mixture source [50], a direct reaction between Zn and S vapors [51], a seed-epitaxial MOCVD process [52], etc. Other 1D ZnS nanostructures and doped 1D ZnS nanostructures have been successfully synthesized via various methods [13]. In this section, we present the recent progresses achieved by us in relation to the synthesis, characterization, and property studies of 1D ZnS nanostructures.

Ordered ZnS nanotubes [43]

We introduced the PAA membranes into an MOCVD process to fabricate well-aligned ZnS nanotube arrays without using any catalysts. Different from conventional thermal evaporation and CVD methods in which ZnS powders or ZnS-based mixture have always been adopted as source materials, herein low-pressure thermal decomposition of zinc bis(diethyldithiocarbamate) [$Zn(S_2CNEt_2)_2$] was employed. The top-down view of the highly aligned nanotubes can be seen in Fig. 5a. The nanotubes, several tens of microns long, are arranged in a continuous, parallel, and well-ordered way. The pores of the nano-

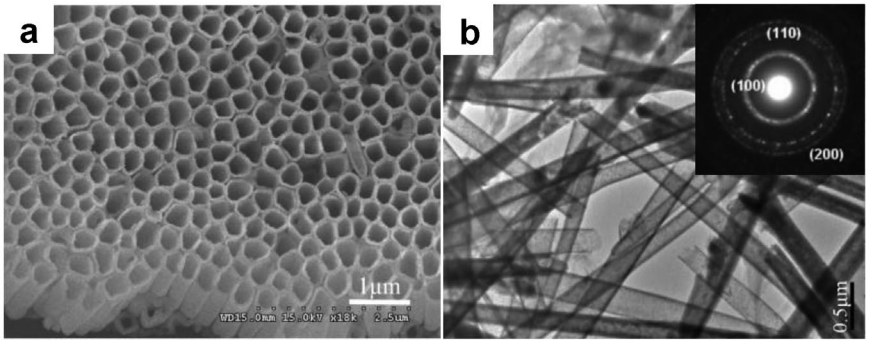

Fig. 5 SEM image and TEM image of ZnS nanotubes. Reproduced from *Mater. Chem. Phys.* **100**, 281 (2006). Copyright © 2006, Elsevier [43].

tubes are straight, with a smooth surface and a diameter of ~140–250 nm, which corresponds to the pore diameter of the used PAA template. The wall thicknesses of the nanotubes are uniform, and the compactness is quite high, about 8.1×10^8 pores/cm^2. Transmission electron microscopy (TEM) and selected-area electron diffraction (SAED) results show that the nanotubes are polycrystalline, Fig. 5b. A strong blue–green emission centered at 510 nm is observed. Due to its low temperature and versatility, this MOCVD-template method might present a new and easy approach to fabricate nanotubes from various kinds of sulfides. Such nanotubes grown without catalyst may have promising applications in optical, electric, and gas sensing nanodevices [43].

Size-tunable ZnS tetrapods [52]

The ZnS tetrapods were synthesized utilizing a one-step seed-epitaxial MOCVD approach and using cubic CdSe nanocrystals as the seeds. In these experiments, single-crystalline p-type Si substrates covered with cubic CdSe nanocrystals (as the collecting substrates) were placed in a high-temperature furnace zone, and the distances between the substrates and $Zn(S_2CNEt_2)_2$ powder were about 17, 19, 23, and 25 cm for samples A, B, C, and D, respectively. And the ZnS tetrapods with different diameters were formed. The characteristic morphologies of the ZnS tetrapods can be seen in the SEM images. The four arms of the tetrapods are of the same size. Their surfaces are smooth. The angles between the arms are nearly the same, analogous to the 3D structure of macular methane. Apart from the tetrapod-like nanocrystals, monopods, bipods, tripods, multipods, and pods, congeries were also obtained. Furthermore, the sizes of the nanopods can be easily tuned by changing the distances between the substrates and precursors, while the temperatures may be kept almost the same. With increasing distances, the as-grown ZnS nanopods with different mean diameters were sorted into different groups: 250 nm (sample A), 180 nm (sample B), 100 nm (sample C), and 70 nm (sample D), as shown in Fig. 6. X-ray diffraction (XRD) measurement shows that the products are wurtzite (hexagonal) structured ZnS. Careful TEM examinations shed additional light on the structure of the tetrapods (Fig. 7). The high-resolution TEM (HR-TEM) and SAED examinations verify that all branches of each tetrapod are structurally uniform and are single crystals that grow along the [0001] direction. From the energy-dispersive

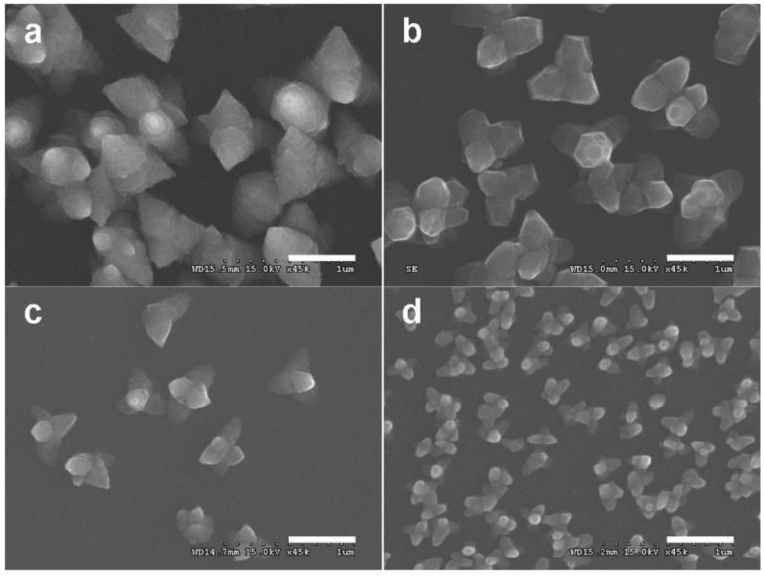

Fig. 6 SEM images of ZnS tetrapods of different sizes: in average (a) 250 nm; (b) 180 nm; (c) 100 nm; and (d) 70 nm, all scale bars are 500 nm. Reproduced from *J. Solid State Chem.* **181**, 950 (2008). Copyright © 2008, Elsevier [52].

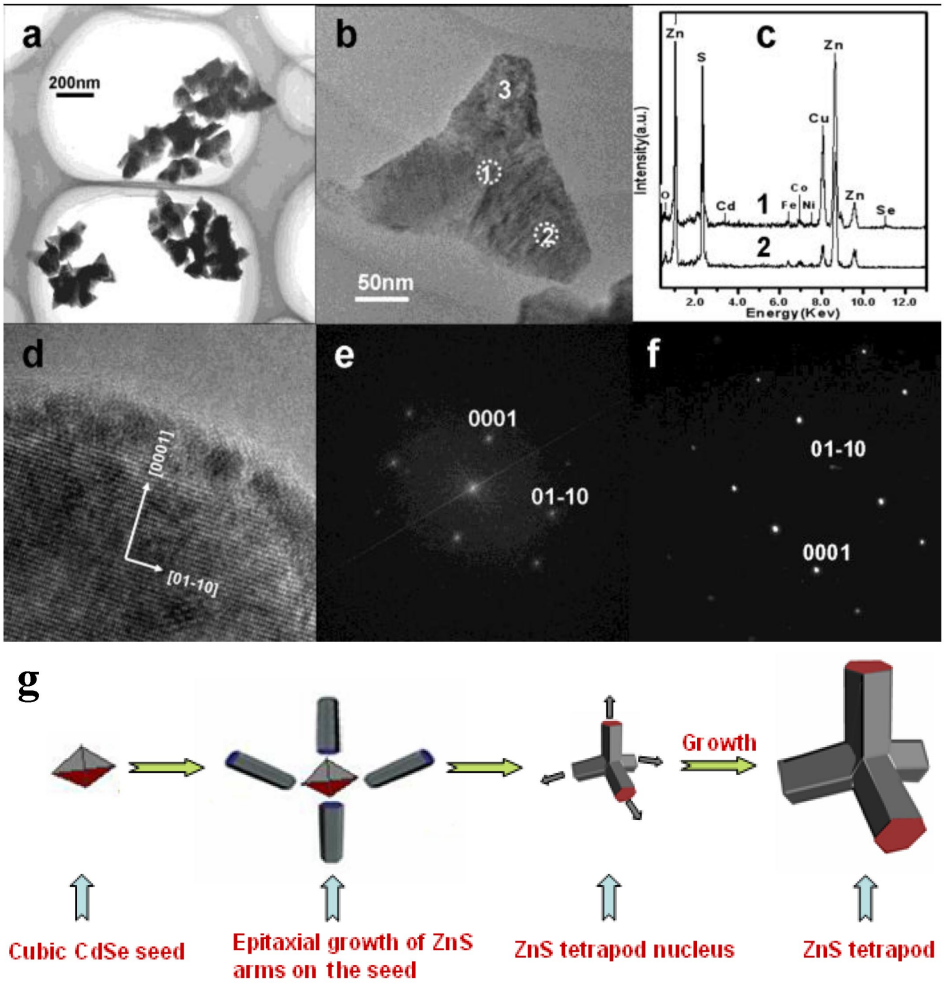

Fig. 7 (a, b) TEM images of ZnS tetrapods (70 nm); (c) EDS spectra taken from regions 1 and 2 in (b); (d, e) HR-TEM image and corresponding FFT image on region 3; (f) SAED pattern taken from region 2; (g) Proposed growth mechanism of ZnS tetrapods. Reproduced from *J. Solid State Chem.* **181**, 950 (2008). Copyright © 2008, Elsevier [52].

spectrometry (EDS) analysis, only Zn and S signals were found in the projected branch region; in the projected core region, Cd and Se were also detected, which confirmed that the CdSe nanocrystals were in the cores of tetrapod-like structure. On the basis of data analysis, the formation process of the tetrapod-like ZnS nanopods was proposed, a schematic description of which is given in Fig. 7g. In the beginning, the $Zn(S_2CNEt_2)_2$ vapor generated under thermal evaporation is transported by the carrier gas to the substrates located at the high-temperature zone, then it decomposes to form ZnS vapor. Owing to a required excess energy for nucleation, the newly arrived ZnS vapor prefers to deposit on the CdSe seeds, and the epitaxial growth of wurtzite-structured arms occurs on the seeds. Four wurtzite arms grow equivalently out of the four {111} equivalent faces of a tetrahedral zinc blende seeds, finally resulting in a tetrapod-shaped ZnS nanocrystal. This behavior is well known, and is due to the small energy difference between stacking sequences along the growth direction. From zone A to D, the distance between the substrates and precursors increases, and the degree of supersaturations and diffusion rate of ZnS molecules decreases. This results in the formation of smaller tetrapods [52].

ZnS nanoawls [53]

Different from ZnS nanotubes and tetrapods, single-crystalline ZnS nanoawls were fabricated at high yield under a simple two-step pressure-controlled vapor-phase deposition, not an MOCVD process, at a relatively high temperature of 800 °C using a mixture of commercial ZnS and SnO_2, and graphite powders as precursors. Single-crystalline Si wafers covered with Ag were used as deposition substrates. As shown in Fig. 8a, awl-holders exhibited hexagonal and rectangular characteristics and have an average diameter of 700 nm, and the awl tips on the top have a diameter of 100–200 nm. HR-TEM and SAED results (Figs. 8b,c) indicate that the holder and the tip of the nanoawl are both single crystals growing along the [120] direction. A possible two-stage growth mechanism was proposed, where the growth could be separated into two stages. The first stage is the growth of the nanorods along the [120] direction, which is governed by the vapor–solid (VS) mechanism. Subsequently, the second stage involved the growth of narrow awl tips on the holders. The nanotips form when the working pressure is suddenly decreased at the beginning of the slow cooling process. A stable and strong green emission band centered at 513 nm and a weaker blue emission band centered at 447 nm are seen from the bulk nanoawls. We suggest that the blue emission at 447 nm may be ascribed to the transitions involving vacancy states, while the observable green emission is caused by some self-activated centers, vacancy states, or interstitial states associated with the peculiar nanostructures [53].

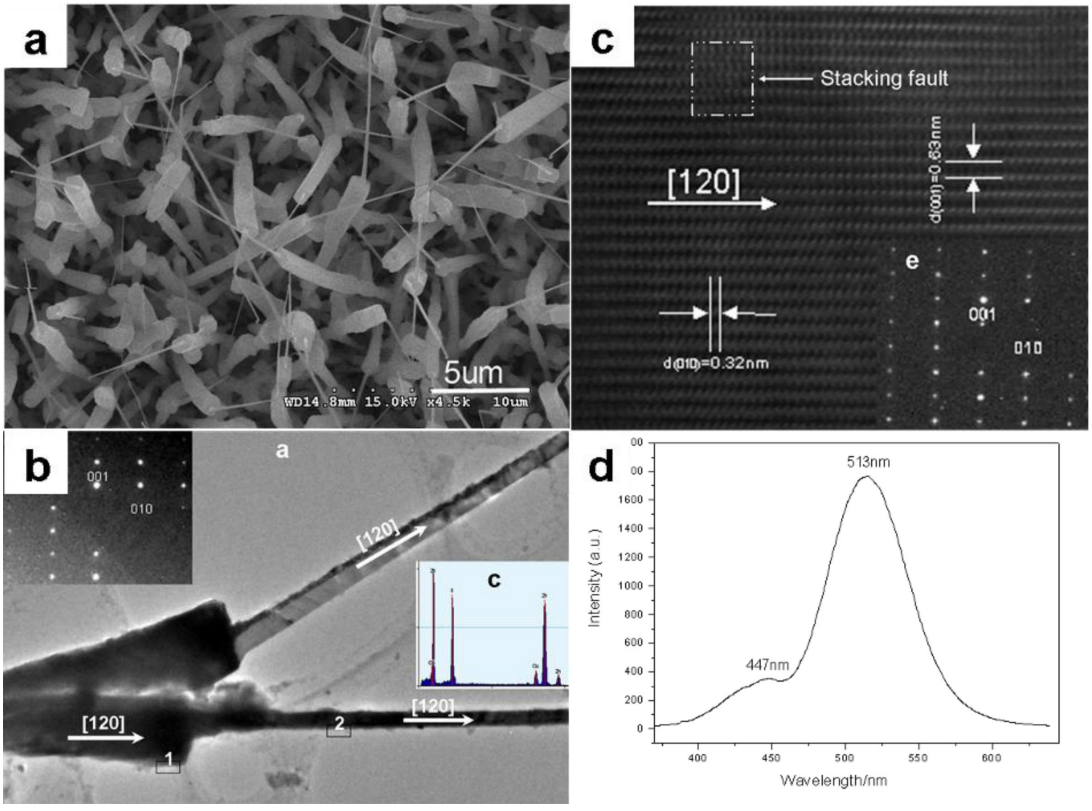

Fig. 8 (a) SEM image of the ZnS nanoawls; (b) TEM image, corresponding SAED pattern and EDS spectrum of the ZnS nanoawls; (c) HR-TEM image taken from region 2 of (b); and (d) photoluminescence (PL) spectrum of the ZnS nanoawls using a He–Cd laser with an excitation wavelength of 325 nm. Reproduced from *Cryst. Growth. Des.* **7**, 1388 (2007). Copyright © 2007, American Chemical Society [53].

ZnS ultrafine nanobelts [54]

Unlike 1D nanostructures (nanotubes, tetrapods, and nanoawls) discussed above, the nanobelts have a rectangular cross-section with well-defined geometry and high crystallinity. After discovery by Zhong Lin Wang's group in 2001, nanobelts have become one of the most interesting objects. Single-crystalline, narrow-size-distribution ultrafine ZnS nanobelts were synthesized at a high yield by controlling the evaporation and agglomeration rates during the synthesis. What should be mentioned is that the synthesis of ultrafine ZnS nanobelts was accomplished in a vertical induction furnace, which is different from that used for ZnS nanotubes, nanoawls, and tetrapods. During the synthesis, we used a mixture of commercial ZnS powders, C nanopowders, and S powders as precursors, and Ar gas of 40 sccm as a protecting medium and carrying gas. The furnace temperature and growth time were 1000 °C and 60 min, respectively (details in ref. [54]).

The SEM result reveals that the nanobelts are several tens of micrometers in length (Fig. 9a). Each belt has a uniform width over its entire length. A typical width of the nanobelts is ~5–30 nm, being peaked at ~10–20 nm. The belt thickness varies with width and is typically of only several nanometers. Figure 9b shows a typical HR-TEM image of a single ZnS nanobelt. It can be seen that a thin amorphous carbon layer coats the side belt surfaces. This thin amorphous carbon layer arises not from a TEM

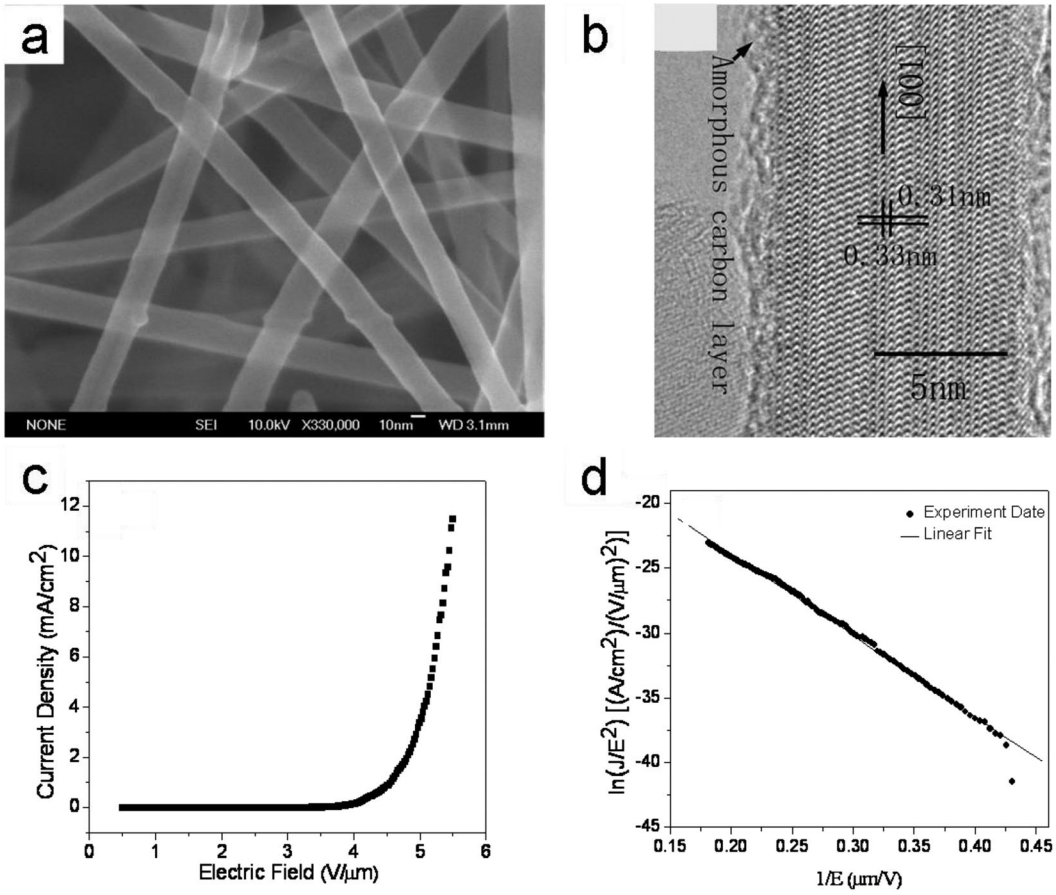

Fig. 9 (a) SEM image of ultrafine ZnS nanobelts; (b) Lattice-resolved HR-TEM image taken from an individual nanobelt 9 nm wide; (c, d) Field-emission (FE) performances of ZnS nanobelts: (c) FE current density vs. the applied field (J–E) curve and (d) corresponding F–N plot. Reproduced from *Adv. Mater.* **19**, 2593 (2007). Copyright © 2007, Wiley-VCH [54].

mesh, but forms during the belt growth. It serves as a blocker for the belt width and thickness increase more effectively than for its length increase, since the growth proceeds along the [001] direction of ZnS. This orientation is the fastest and easiest growth direction according to the well-established ZnS crystallization kinetics. All these phenomena lead to the ultrafine ZnS nanobelt formation. The nanobelts grow along the [001] direction, and typically have no defects, e.g., stacking faults or dislocations. We have carried out FE measurements on these ultrafine ZnS nanobelts and found that they possess excellent performances: a turn-on field of about 3.47 V/μm at a current density of 10 mA/cm^2, and the emission current density of about 11.5 mA/cm^2 at a macroscopic field of 5.5 mA/cm^2, as shown in Fig. 9c. Figure 9d shows the Fowler–Nordheim (F–N) plot for the nanobelts, which fits well to the line. As obtained from the slope of the fitted straight line in Fig. 9d, the nanobelts have a high field-enhancement factor (β) of 2.01×10^3. These data suggest that the present nanobelts are highly valuable field emitters that rival previously reported ZnO, ZnS, Si, SiC, and AlN nanowires/nanobelts and CNT emitters [54,55].

ZnS nanobelt quasi-arrays [44]

These quasi-aligned ZnS nanobelt arrays were fabricated through a non-catalytic and template-free thermal evaporation process. They are not only aligned on the micro/macroscopic scales but also display similar crystallographic orientations of their growth axes. The SEM observations reveal that a typical length of the belts is several tens-to-hundreds of micrometers, as shown in Fig. 10a. The belts form in bundles, and within a bundle they are quasi-aligned. In many cases, even perfectly parallel ensembles are visible. Figure 10b presents a typical TEM image of an array of parallel nanobelts. The inset shows an SAED pattern from the entire bundle. The similar orientation of all nanobelts within the bundle along the [001] direction is documented. HR-TEM images of an individual nanobelt display the defect-free (001) lattice plane of wurtzite ZnS with an inter-planar d-spacing of 0.62 nm, suggesting that the growth direction is [001]. We have carried out FE measurements on these structures and found that they have much improved properties as compared to random nanowires: a low turn-on field (~3.55 V/μm) and a high field-enhancement factor ~1850). The emission characteristic plots are shown in Figs. 10c,d. The emission current density reaches 14.6 mA/cm^2 at a macroscopic field of 5.5 V/μm. This value is more that 20 times higher than for randomly distributed ZnS nanobelts. Figure 10d shows variations of emission current density of a belt ensemble within 4 h under an applied field of 5 V/μm. No notable current density degradation was observed, and the emission current fluctuations were as low as ~2.6 %, proving the high stability of the ZnS-aligned emitters [44]. To date, there have been only a few reports that deal with FE properties of ZnS nanostructures. Table 2 lists some important FE parameters of 1D ZnS nanostructures reported so far.

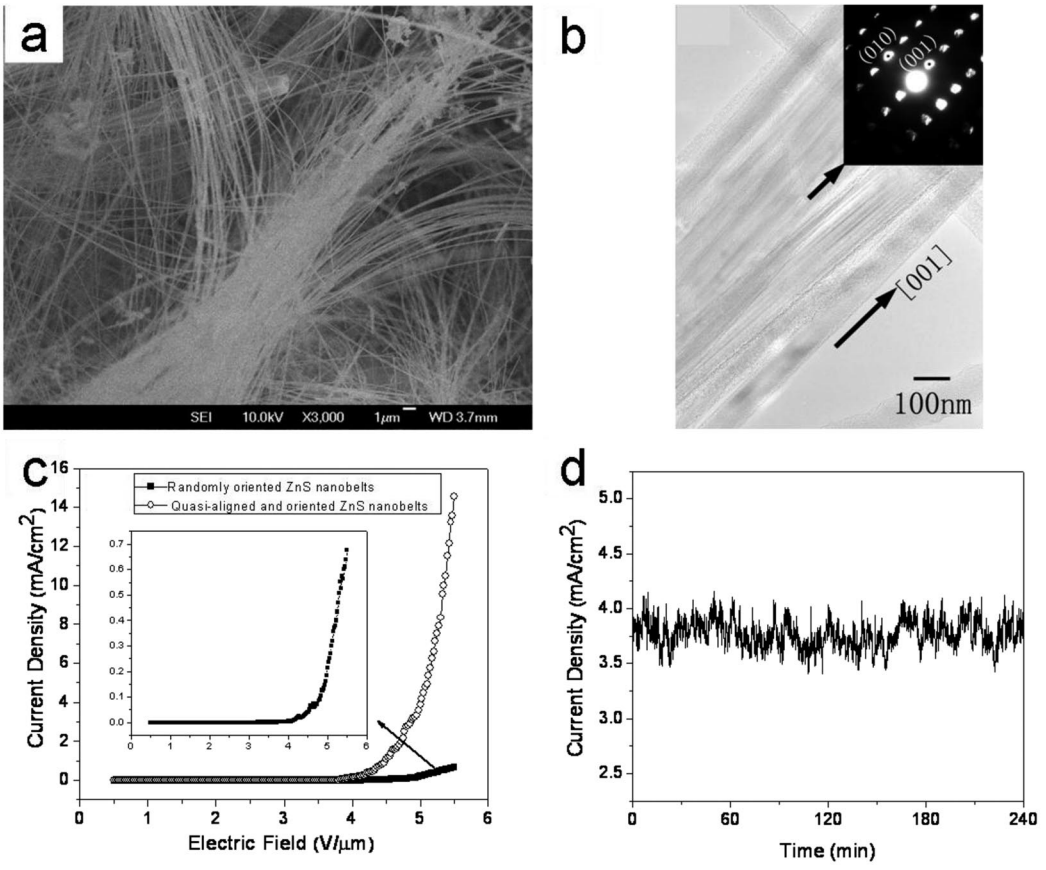

Fig. 10 (a) SEM image of ZnS nanostructures displaying their quasi-aligned belt-like structures; (b) Typical TEM image of a ZnS nanobelt array. The inset is a SAED pattern taken from the entire bunch showing uniform alignment along [001]-ZnS orientation; (c) J–E plots of quasi-aligned and randomly oriented ZnS nanobelts. The inset is a magnified J–E curve for random ZnS nanobelts; (d) A J-t plot of quasi-aligned ZnS nanobelt arrays at an applied electric field of 5 V/μm. Reproduced from *Chem. Commun.* 3048 (2007). Copyright © 2007, Royal Society of Chemistry [44].

Table 2 Key performance parameters of 1D ZnS nanostructures reported in the literature.

ZnS emitters	Synthesis method	Turn-on field (V/μm)	β	Ref.
Nanobelts	Chemical vapor deposition	3.47 at 10 mA/cm^2	2.01×10^3	54
Nanobelts	Thermal evaporation	3.55 at 10 mA/cm^2	1.85×10^3	44
Branched nanostructures	Thermal evaporation	3.77 at 10 mA/cm^2	2182	56
Nanowires	Thermal evaporation	5.46 at 0.1 mA/cm^2	1319	57
Nanowires	Vapor phase deposition	11.7 at 0.1 mA/cm^2	522	58
Nanorods	Radio frequency magnetron sputtering technique	2.9–6.3 at 2.452 μA/cm^2	420–105	59
Tetrapod tree-like heterostructures	Thermal evaporation	2.66 at 0.1 μA/cm^2	2600	60

1D CdS nanostructures

Various 1D CdS nanostructures have been synthesized. For example, CdS nanowires were prepared by an MOCVD process [31], a laser-assisted catalytic growth (LCG) method [61], an electrochemical technique [62], a virus-based toolkit [63], thermal evaporation [64], CVD [65], chemical bath deposition [66], electrochemically induced deposition [67], etc. CdS nanotubes were fabricated using a micelle-template-interface reaction route [68], a CVD-template method [69], chemical bath deposition [70], microwave-template synthesis [71], sacrificial template growth [72], etc. CdS nanobelts or nanoribbons were made through thermal evaporation [73–75], a vapor transport [76], a CVD process [77], PLD [78], etc. Other 1D CdS nanostructures and doped 1D CdS nanostructures have successfully been fabricated via various methods [79,80]. In this section, we present the authors' recent progresses in the synthesis, characterization, and property measurements of 1D CdS nanostructures.

CdS rocket-like tetrapodal nanorods [80]

Taking the idea of epitaxial growth, we fabricated the rocket-like CdS tetrapods (RTPs) via a one-step seed-epitaxial MOCVD approach by thermal decomposition of $Cd(S_2CNEt_2)_2$ powders using Ag particles and cubic CdSe nanocrystals as catalysts. This bottom-up method uses Ag particles to initiate and guide the preferential orientation of the axial nanorods, while the epitaxial growth of wurtzite-structured branches occurs on the cubic CdSe seeds. The SEM images (Figs. 11a,b) show that the as-synthesized CdS nanostructures appear gray and evenly cover the Si deposition substrate. Each nanorod of CdS RTPs consists of three branches of 500 nm in length, and the stem of 200 nm in diameter. The nanorods keep their threefold array of parallel branches around the central stems. Unlike the traditional tetrapod structures, the central stem was longer than the branches and passed through the center of the tetrapod. These structural characters are easily noticed while looking at the TEM image (Fig. 11c). The HR-TEM

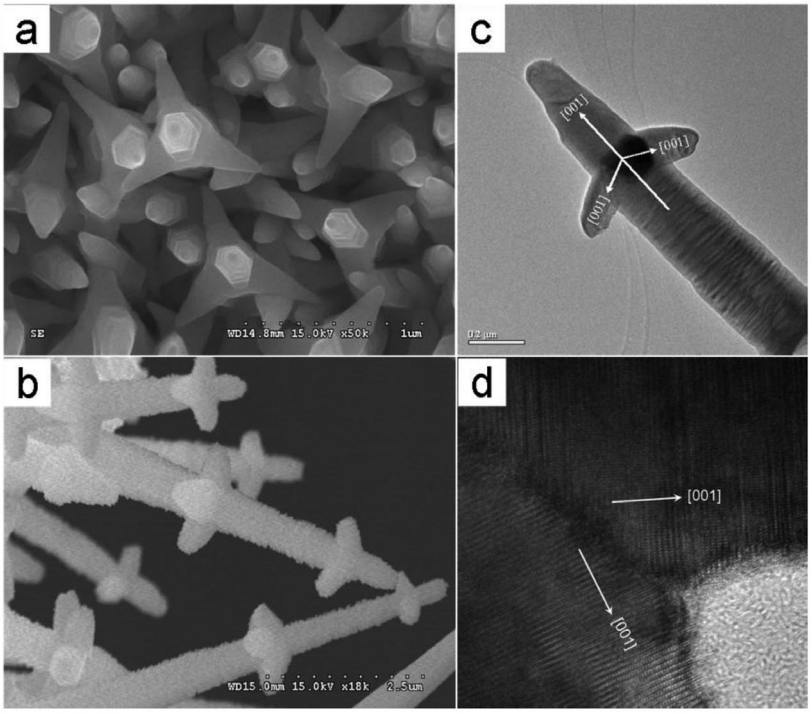

Fig. 11 (a) SEM image of CdS RTPs; (b) SEM image of two-level RTPs; (c) TEM image of a CdS RTP; and (d) HR-TEM image of the interface between the branch and the central nanorod of the CdS RTP. Reproduced from *Cryst. Growth Des.* **7**, 488 (2007). Copyright © 2007, American Chemical Society [80].

image and SAED pattern indicate that the stem and the branches of the CdS RTP structure have a single-crystalline structure and grow along the [001] direction. In order to understand the formation mechanism of the CdS RTPs, we have conducted additional experiments. These indicated that the Ag particles and cubic CdSe NCs play an important role in the structure formation. (1) Using only Ag particles, highly dense CdS nanoneedles were found to cover the entire substrate (Fig. 12a). The morphology and intrinsic structure are similar to the axis rod of the CdS RTPs. (2) Using only cubic CdSe NCs, some branched CdS nanostructures can be obtained (Fig. 12d), which are similar to the branches of the RTPs. (3) Decreasing the amounts of Ag particles, the quantity of the CdS RTPs is reduced accordingly (Fig. 12e). (4) Using wurtzite NCs, CdS nanoneedles were obtained which showed a similar morphology to those formed in the absence of the seeds. (5) Using mixed NCs, CdS nanoneedles and RTPs were found to exist (Fig. 12f), also no arms were observed on some CdS nanorods. These results confirm that Ag particles and the zinc blende CdSe seeds are crucial to the preparation of CdS RTPs using the seed-epitaxial method. On the basis of the above analysis, the formation process of the CdS RTPs is pro-

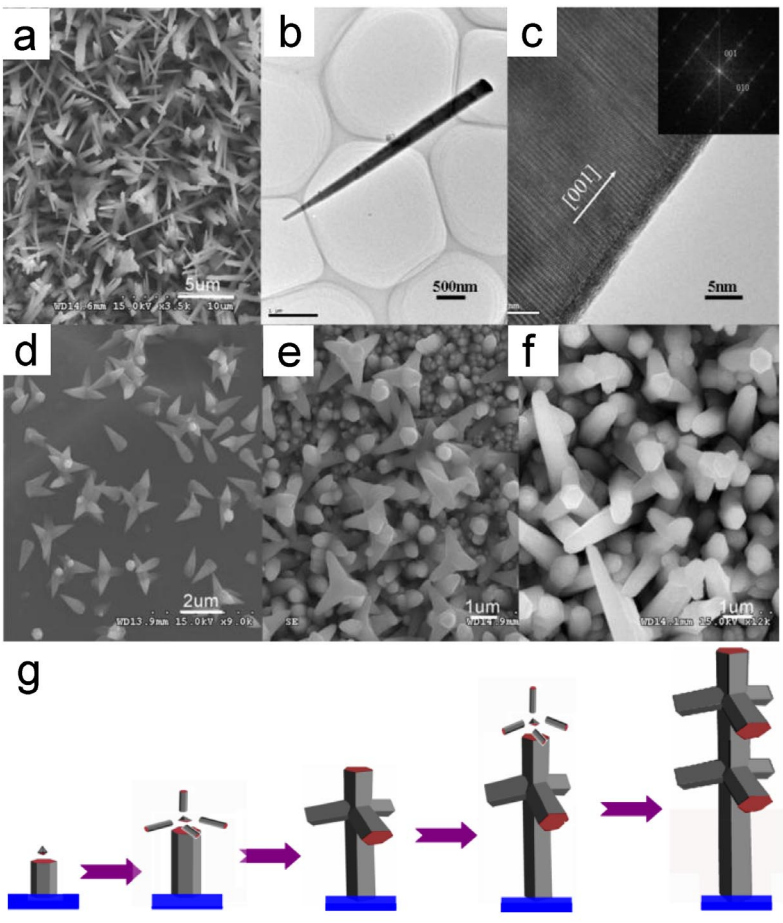

Fig. 12 (a) SEM image, (b) TEM image, (c) HR-TEM image and corresponding FFT pattern of CdS nanoneedles synthesized using Ag particles; SEM images of CdS nanostructures synthesized (d) using only cubic CdSe NCs, (e) using nearly half of the Ag particles used in (a) and cubic CdSe NCs, (f) using as many Ag particles as used in (a) and mixed structures of CdSe NCs (wurtzite/zinc blende = 2); and (g) schematic diagram for the growth mechanism of the CdS RTPs. Reproduced from *Cryst. Growth Des.* **7**, 488 (2007). Copyright © 2007, American Chemical Society [80].

posed, a schematic description of which is given in Fig 12g, and detailed growth mechanism is discussed in ref. [80].

CdS ordered nanostructure arrays [81]

Different from CdS RTPs, the CdS nanostructure arrays were synthesized through a two-step MOCVD process using Au nanocrystals as catalysts. Home-made $Cd(S_2CNEt_2)_2$ powders were put in a quartz boat at the upstream end of the tube furnace. Several p-type Si substrates covered with Au nanocrystals were placed in the high-temperature zone to collect the products, and the distances between the substrates and left margin of the furnace were ~16, 18, 23, 25, and 27 cm for sample a, sample b, sample c, sample d and sample e, respectively. First, the furnace was rapidly heated to 650 °C and kept at this temperature for 120 min and then cooled to room temperature. Second, the quartz boat was taken out of the furnace and filled with the $Cd(S_2CNEt_2)_2$ powders again and placed back into the furnace. The furnace was heated to 420 °C, and held at that temperature for 240 min. All the growths were carried out under a N_2 flow of 60 sccm at a base pressure of 100 Pa. The nanomaterials were collected on the Si wafers at different positions in the furnace [81].

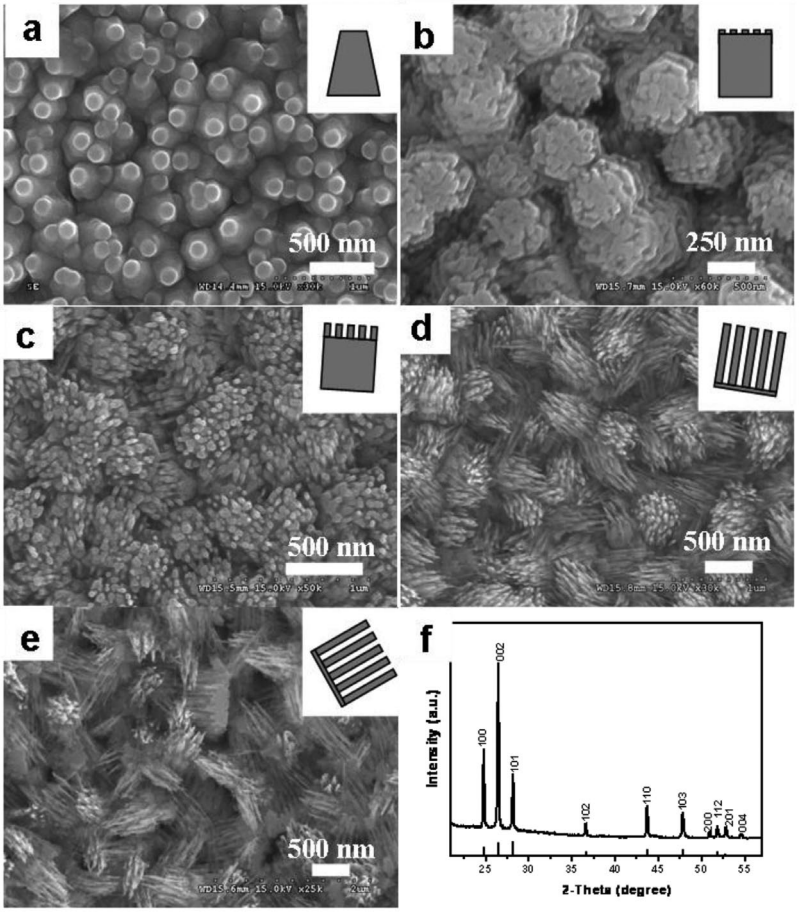

Fig. 13 Typical SEM images and corresponding geometric sketches of several CdS nanostructures: (a) well-aligned truncated nanocone arrays (sample a); (b) well-aligned nanorod arrays (sample b); (c) well-aligned cleft nanorod arrays (sample c); (d) quasi-aligned nanowire arrays (sample d); (e) nanowire arrays (sample e); and (f) XRD pattern of the as-prepared CdS nanostructures (sample a). Reproduced from *ACS Nano* **3**, 949 (2009). Copyright © 2009, American Chemical Society [81].

The SEM images show that the ordered arrays of CdS nanostructures uniformly and compactly cover the entire substrates, and the morphologies and alignments of nanostructure arrays are quite different for different distances between the precursors and a substrate. With increasing distances, the morphologies of CdS nanostructures are varied from well-aligned truncated nanocone arrays (Fig. 13a), well-aligned nanorod arrays (Fig. 13b), well-aligned cleft nanorod arrays (Fig. 13c), quasi-aligned nanowire arrays (Fig. 13d), to nanowire arrays (Fig. 13e). The temperatures of the different zones are almost the same. The XRD pattern of the CdS nanostructures (sample a) is shown in Fig. 13f. All the diffraction peaks can be readily indexed to a hexagonal wurtzite-structured CdS with the lattice parameters of a = 4.14 Å, c = 6.72 Å. The detailed microstructures of ordered CdS nanostructures were further studied by TEM. As can be derived from the SAED and HR-TEM images, all the nanostructures are single crystals grown along the [001] direction (Fig. 14) [81].

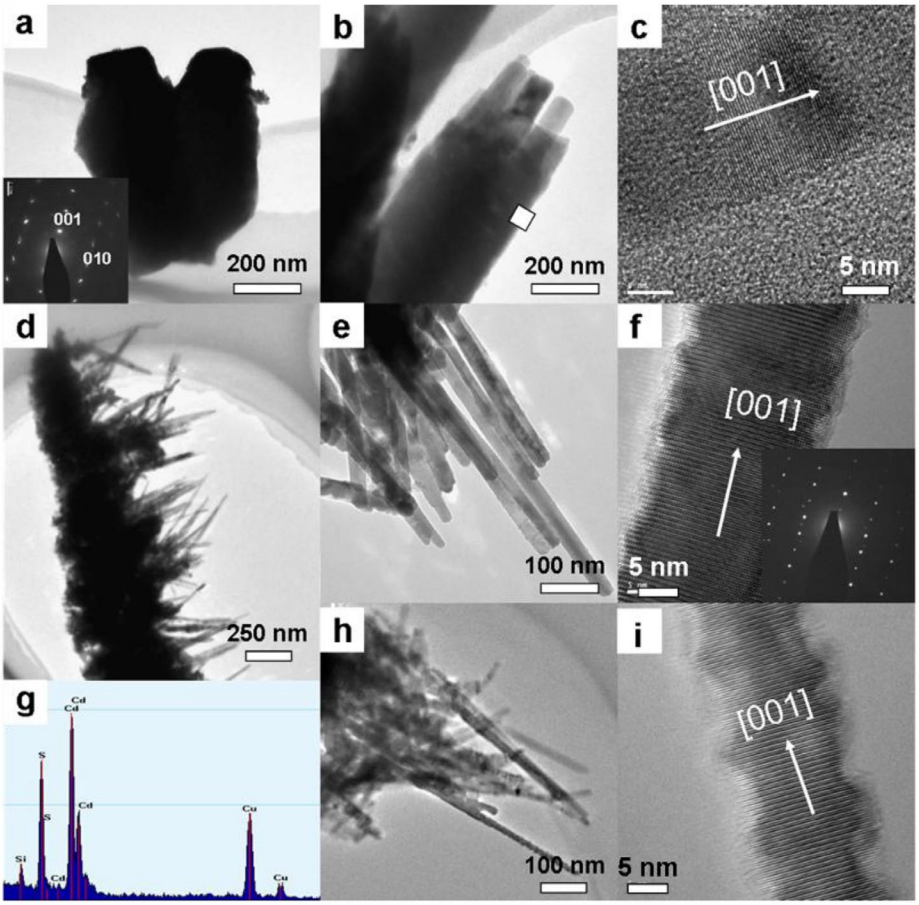

Fig. 14 TEM images of various CdS nanostructures: (a) TEM image and ED pattern (inset) of the truncated nanocones (sample a); (b, c) TEM image and HR-TEM image of the cleft nanorods (sample c); (d–g) TEM image, HR-TEM image, and EDS spectrum of the quasi-aligned nanowire arrays (sample d); (h, i) TEM image and HR-TEM image of the nanowire arrays (sample e). Reproduced from *ACS Nano* **3**, 949 (2009). Copyright © 2009, American Chemical Society [41].

The uniform dimensions and good crystallinities of the obtained CdS nanostructure arrays indicate that the stimulated emission or lasing under high excitation may be realized in them. Figure 15a

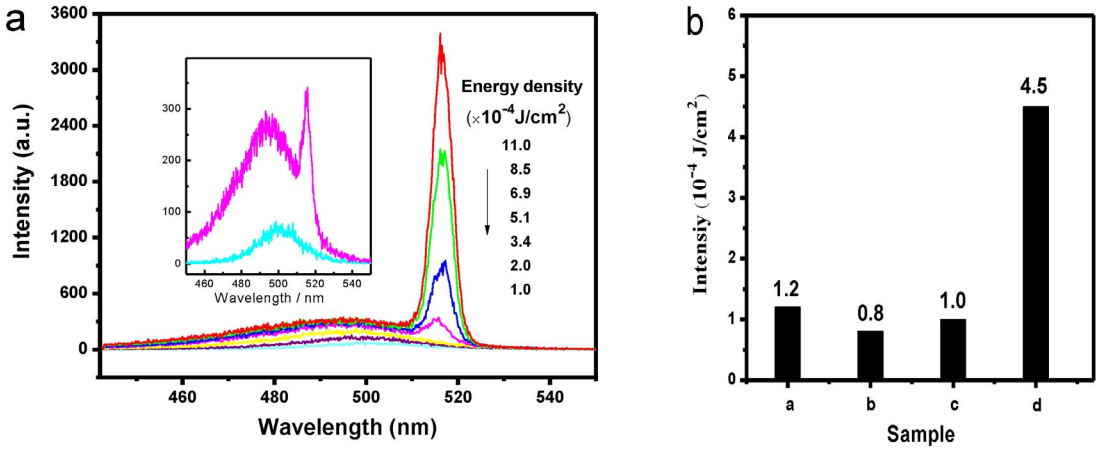

Fig. 15 (a) Power-dependent PL spectra of the CdS nanowire arrays (sample d) excited by a femtosecond laser with various excitation power densities at room temperature; the inset is the enlargement of the two curves at 1.0×10^{-4} and 5.1×10^{-4} J/cm^2; (b) Threshold for lasing of the as-prepared CdS nanostructures (samples a–d). Reproduced from *ACS Nano* **3**, 949 (2009). Copyright © 2009, American Chemical Society [81].

displays the power-dependent photoluminescence (PL) spectra of CdS nanorods (sample d) excited by the femtosecond laser pulses with various power densities at room temperature. At a low excitation intensity, a broad and weak band appears at 500.1 nm (2.480 eV), which is attributed to the spontaneous exciton transition at the CdS bandgap. When the excitation power density increases to ~6.1×10^{-4} J/cm^2, a new side band appears at 515.6 nm (2.405 eV), existing at the lower energy side of the broad main band. This side band with a ~75 meV red-shift is attributed to the E-2LO phonon band, since 2LO phonon energy (ca. 76 meV) is close to the observed red-shift and larger than the available thermal energy at room temperature (~26 meV). This peak has a full width at a half-maximum (FWHM) of 5 nm, which is less than for spontaneous exciton emission, and its output intensity increases rapidly, clearly indicating a lasing action. Figure 15b shows the lasing threshold of the as-prepared CdS nanostructures. It is clear that the well-aligned nanorod arrays (sample b) have the lower threshold (0.8×10^{-4} J/cm^2), compared to the well-aligned truncated nanocone arrays (1.2×10^{-4} J/cm^2), well-aligned cleft-nanorod arrays (1.0×10^{-4} J/cm^2) and quasi-aligned nanowire arrays (4.5×10^{-4} J/cm^2). We do not observe the stimulated emission phenomenon in the nanowire arrays (sample e). We suggest that the lasing threshold is mainly dependent on the orientation of an array. Sample a, b, and c have similar orientations, which result in similar lower thresholds. Sample d has the poorest orientation, leading to the higher threshold. When the alignment deteriorates, no stimulated emission is observed [81].

The curves of the emission current density vs. the applied field curve (J–E) from the five samples are shown in Fig. 16a. The quasi-aligned nanowire arrays (sample d) have the best FE properties with the lowest turn-on field of 12.2 V/μm, the lowest threshold field of 15.7 V/μm and the highest J at the same E value. Meanwhile, the turn-on fields from the other samples are 14.9, 14.0, 13.4, and 21.9 V/μm. In comparison to the FE characteristics of CdS nanowire arrays reported by other researchers, the E_{to} value of sample d is lower, but the value of sample e is higher. This discrepancy may be due to a smaller number of the present emitter tips resulting from the coalescence of nanowires. The linear variation of ln(J/E^2) with (1/E) (F–N plot), Fig. 16b, implies that the electron emission from CdS nanorod arrays follows the F–N behavior. Quasi-aligned nanowire arrays (sample d) have the highest β value (555) compared to sample a (384), sample b (408), sample c (450), and sample e (129). The excellent FE properties and high β of sample d are likely attributed to the higher aspect ratio (or smaller emitter radius) than those of samples a, b, and c, and the better alignment (see Fig. 13) than that of sample e. In summary, the 1D CdS nanostructures of various types displayed notable differences in stimu-

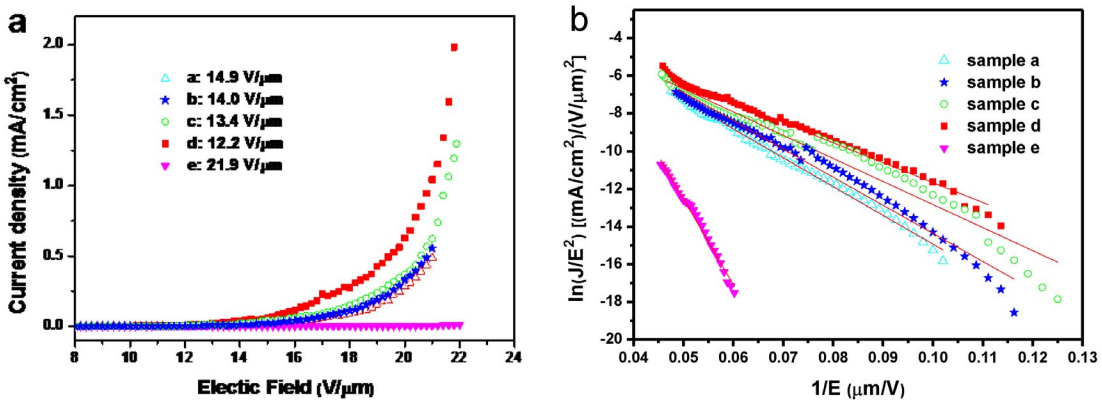

Fig. 16 FE properties of the as-grown CdS nanostructures. (a) FE current density vs. the applied field (J–E) curves from the five samples at a working distance of 50 μm; (b) the corresponding F–N plots roughly showing linear dependence. Reproduced from *ACS Nano* **3**, 949 (2009), Copyright © 2009, American Chemical Society [81].

lated and FE performances. The stimulated emission strongly correlated with the structure alignment: the better the alignment, the lower the threshold. Both the alignments and aspect ratios greatly affected the FE properties: the CdS emitters of higher aspect ratio and better alignment exhibited better FE performance. Thus, the well-aligned CdS nanorod arrays had the lower threshold for stimulated emission, and quasi-aligned nanowire arrays produced the higher FE current and possessed the lower turn-on fields [81].

Morphology-tunable CdS micro/nanostructures [82]

The synthesis of CdS micro- and nanostructures was conducted in a horizontal tube furnace with a 40-nm outer-diameter quartz tube mounted inside. In short, commercial CdS and graphite powders with a weight ratio of 2:1 were mixed, ground, and then loaded on an alumina boat and positioned at the center of the tube, while several single-crystal Si wafers, cleaned by a standard procedure and covered with Au nanoparticles, were placed downstream to act as deposition substrates. The distances between the substrate and the sources were ~20 and ~22 cm for samples a, c and samples b, d, respectively. The furnace tube was purged with high-purity Ar for 3 h, prior to heating in order to eliminate any oxygen in the furnace. The flow rate and pressure inside of the tube were kept, respectively, at 100 SCCM and 210 Pa throughout the experiment. The system was rapidly heated to 800 °C (for samples a and b) or 850 °C (for samples c and d) in 10 min and kept at this temperature for 30 min before it was cooled down to room temperature. Four representative samples (a, b, c, and d) were fabricated by varying some experimental parameters, and the detailed growth conditions for these samples are presented in ref. [82].

The representative morphologies and structures of the produced CdS micro/nanostructures were analyzed by SEM. Figure 17a is the SEM image of a product obtained at 800 °C using 20 nm Au nanoparticles as a catalyst. The microrods have diameters of ~500–1200 nm and lengths up to several micrometers, and exhibit hexagon-like cross-sections. With a decrease in the substrate temperature and without using a catalyst, the morphology changes from microrods to nanotips. The SEM image in Fig. 17b shows that the CdS nanotips are composed of branched nanostructures with needle-shaped tips. When the source temperature becomes higher (850 °C), and under use of sputtered 10 nm Au nanocrystals as a catalyst, the sub-microwires are formed. The SEM image (Fig. 17c) shows that the sub-microwires have a relatively uniform diameter of 450 nm and circular cross-section. The diameters can effectively be controlled by varying the substrate temperature (the latter depends on a distance between the sources and substrates). Figure 17d depicts an SEM image of sub-microwires with a diameter of ~200 nm fabricated at a lower substrate temperature (compared to sample c) while keeping the other

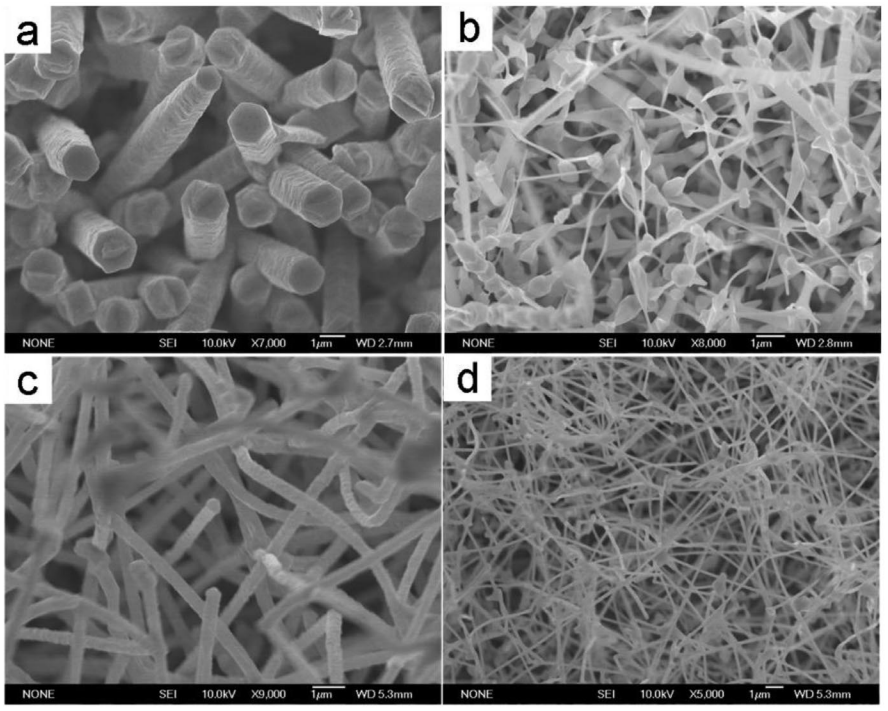

Fig. 17 Typical SEM images of several CdS micro/nanostructures: (a) microrods (sample a); (b) nanotips (sample b); (c) thick sub-microwires (sample c); (d) thin sub-microwires (sample d). Reproduced from *Adv. Funct. Mater.* **19**, 2423 (2009). Copyright © 2009, Wiley-VCH [82].

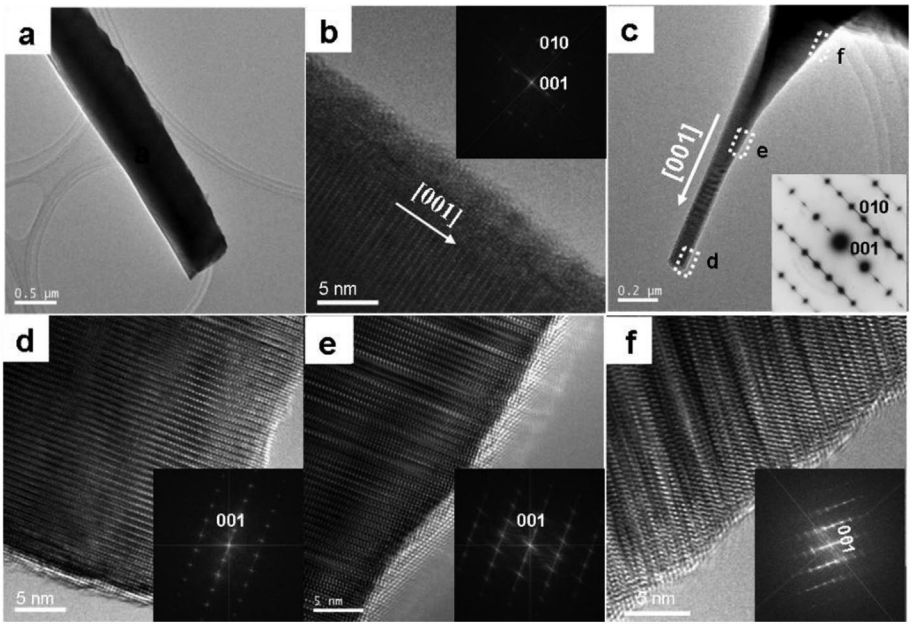

Fig. 18 (a) TEM image, (b) HR-TEM image and corresponding FFT pattern of the CdS microrods; (c) TEM images of nanotips; (d, e, f) HR-TEM images and corresponding FFT patterns recorded in different regions of the nanotip in panel c. Reproduced from *Adv. Funct. Mater.* **19**, 2423 (2009). Copyright © 2009, Wiley-VCH [82].

experimental conditions unchanged. The wire diameters decrease, while the lengths do not change. The detailed microstructures of ordered CdS nanostructures were further studied by TEM. As can be derived from the SAED and HR-TEM images, all the nanostructures are single crystals grown along the [001] direction (Fig. 18). For CdS nanotips, the defect concentration decreases toward the tip-end, as shown in Figs. 18d–f. No metal particles are found at the structure tips, thus the growth mechanism of various CdS nanostructures is attributed to the VS mechanism [82].

Figure 19 illustrates four typical cathodoluminescence (CL) spectra taken from four representative nanostructures: microrods, nanotips, thick and thin sub-microwires. In the CL spectrum of microrods and nanotips, the typical two emission peaks—a weak luminescence emission peak at 525 nm (527 nm for nanotips) and a broad emission at 764 nm (735 nm for nanotips)—are observed, which are assigned to the near-band-edge (NBE) and defect-level (DL) emissions, respectively. In the case of thick and thin sub-microwires, only DL emission is present and no NBE emission is detected. The absence of NBE emission from these sub-microwires demonstrates that they are prone to many intrinsic defects, such as vacancies and interstitials, which form new energy levels, thus hindering the NBE emission. In order to study spatial variation of optical properties and gain an insight into the origin of the DL emission, we have recorded CL spectra at spots with different diameters on a series of individual nanotips. A significant decrease in a DL/NBE intensity ratio is observed along a tapered nanotip toward a smaller diameter part (Fig. 20). We presume that the origin of the DL is related to the peculiar defect distribution in the nanotip bodies, as verified by HR-TEM. The defect concentrations decreased with diameter shrinking, thus the DL emissions also diminished [82].

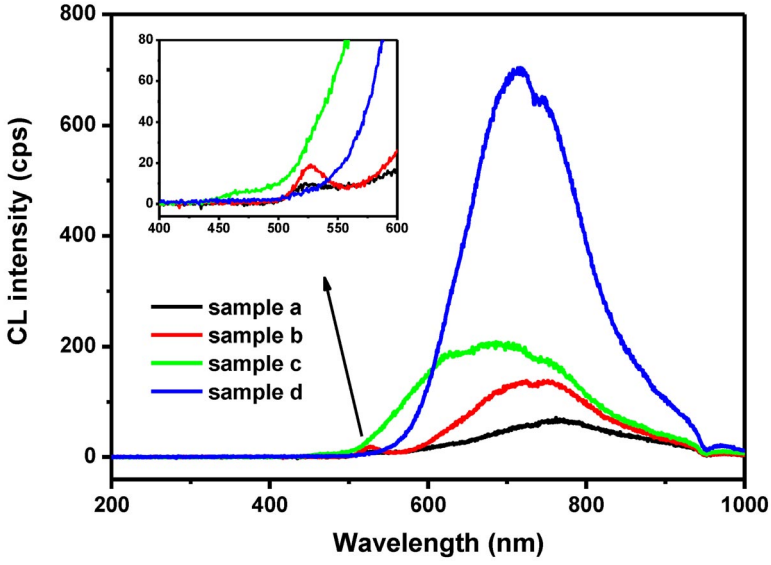

Fig. 19 Room-temperature CL spectra of the CdS microrods (sample a), nanotips (sample b), thick sub-microwires (sample c), and thin sub-microwires (sample d) at an accelerating voltage of 10 kV. The inset highlights the spectra in the range of 400–600 nm. Reproduced from *Adv. Funct. Mater.* **19**, 2423 (2009). Copyright © 2009, Wiley-VCH [82].

As for FE properties, the nanotips have the best FE properties with the lowest turn-on field of 5.28 V/μm, and threshold field of 9.40 V/μm. Meanwhile, the corresponding turn-on fields are 8.95, 10.17, and 8.85 V/μm for other samples, as shown in Fig. 21b. Since the nanotips have much narrower tips compared to other samples, it is reasonable that they show a smaller turn-on field. The inset of Fig. 21a demonstrates the F–N plot, and this plot is approximately linear within the measurement range.

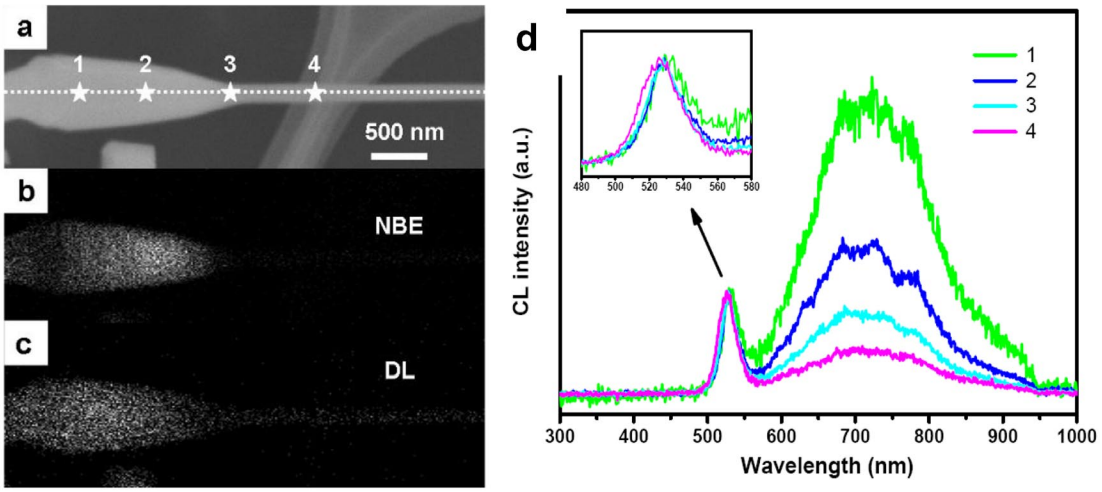

Fig. 20 (a) SEM image of a nanotip with four spots marked by white "stars". (b, c) The corresponding CL images recorded at 530 nm and 725 nm; (d) CL spectra from the four spots using intensity normalized to the NBE emission peak, respectively. The inset highlights the spectra in the range of 480–580 nm. Reproduced from *Adv. Funct. Mater.* **19**, 2423 (2009). Copyright © 2009, Wiley-VCH [82].

This confirms that the electron emission from CdS microstructures follows the F–N behavior. The nanotips have the highest β value (4819) compared to microrods (388), thick microwires (818), and thin microwires (1097), which is more than sufficient for diverse FE applications [82].

Detailed research was conducted to assess the dependence of FE properties on the anode-sample separations. The corresponding J–E curves are plotted in Fig. 21c. The F–N curves are basically fitted to straight lines, indicating that the FE processes still follow the F–N law. When the distance increases from 60 to 180 μm, the turn-on field decreases monotonously from 14.75 to 4.75 V/μm, meanwhile, the threshold field also decreases from 17.1 to 5.97 V/μm. It is found that β increases linearly with the increment of distance d from 60 to 180 μm, as shown in Fig. 21d, which is consistent with the literature. To date, there have been only a few reports that deal with FE properties of CdS nanostructures. Table 3 lists some important FE parameters of 1D CdS nanostructures reported so far.

Table 3 Key performance parameters of 1D CdS nanostructures reported in the literature.

CdS emitters	Synthesis method	Turn-on field (V/μm)	β	Ref.
Nanowires	MOCVD process	12.2 at 10 μA/cm^2	555	81
Nanowires	Solvothermal method	13.4 at 10 μA/cm^2	820	83
Nanowires	Solvothermal method	6.70 at 10 μA/cm^2	—	84
Nanowires	Solution-phase method	—	112, 158	85
Nanowires	MOCVD process	7.8 and 8.9 at 0.1 μA/cm^2	324, 397	86
Nanowires	MOCVD process	2.2 at 10 μA/cm^2	2000	87
Nanotips	Thermal evaporation	5.28 at 10 μA/cm^2	4819	82

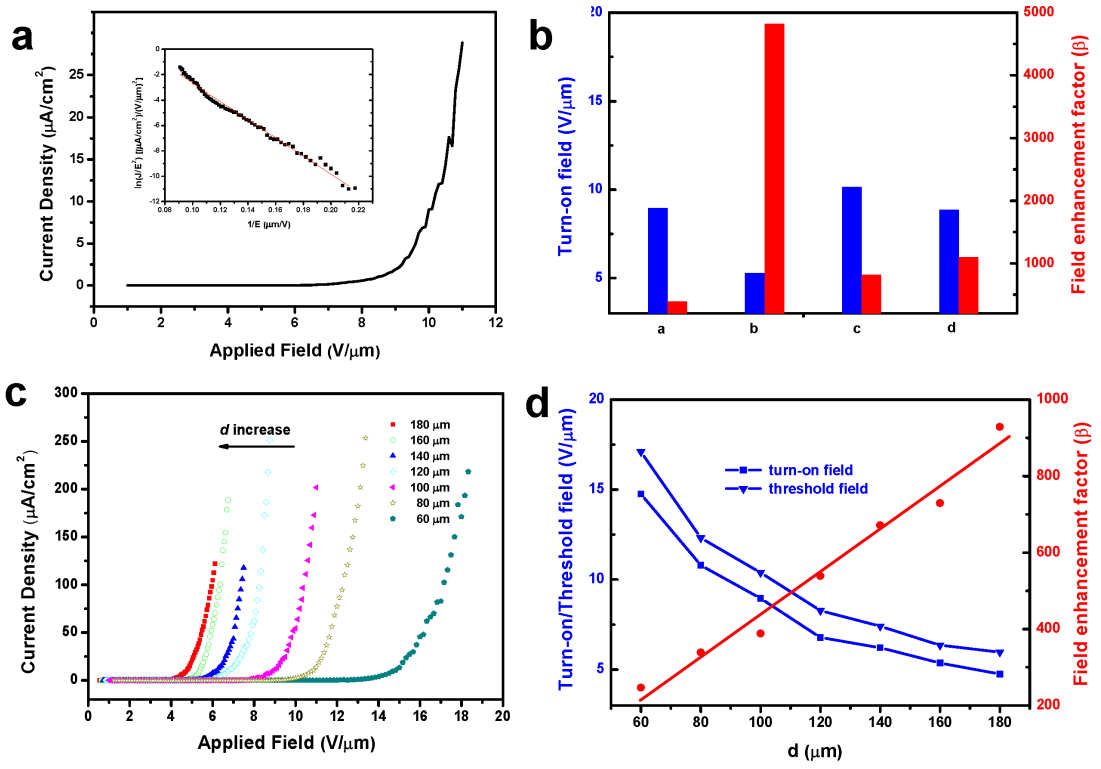

Fig. 21 (a) J–E plots and corresponding F–N plots from CdS nanotips; (b) Turn-on fields and field enhancement factors of these four CdS micro/nanostructures (samples a–d); (c) J–E plots from CdS microrods (sample a) at different anode-sample distances, *d*; (d) variations in turn-on field (at 10 μA/cm^2), threshold field (at 100 μA/cm^2), and field enhancement factor (β) with a distance (*d*); Reproduced from *Adv. Funct. Mater.* **19**, 2423 (2009). Copyright © 2009, Wiley-VCH [82].

1D $Zn_xCd_{1-x}S$ nanostructures

For nano-electronic and -optoelectronic devices, it is very important to fabricate materials with continuously tunable physical properties. Recent advances in ternary semiconductor nanocrystals or films have shown that their bandgaps and thus their optical emissions can be tuned by changing compound stoichiometries. Traditional ternary nanostructures are fabricated by physical evaporation deposition methods or laser ablation-assisted CVD routes [88,89]. These processes involve vapor generation, transport, and deposition of target materials. Such practice, however, inevitably requires high temperatures or high-vacuum laser-ablation operations to generate sufficient amounts of vapor for later deposition. We present a one-step MOCVD approach to prepare single-crystalline ternary $Zn_xCd_{1-x}S$ nanocombs and zigzag nanowires at low temperatures using the mixture of $Zn(S_2CNEt_2)_2$ and $Cd(S_2CNEt_2)_2$ as the sources. Their constituent stoichiometries can be tuned by changing the relative proportion of the precursors.

$Zn_xCd_{1-x}S$ nanocombs [90,91]

Using the mixture of $Zn(S_2CNEt_2)_2$ and $Cd(S_2CNEt_2)_2$ with molar ratio of 1:1 as the sources, $Zn_xCd_{1-x}S$ nanocombs were obtained. These nanocombs are of high purity, and are formed at high yield and under full structural control. An SEM image given in Fig. 22a shows a typical growth of comb-like structure, with one side flat and the other side with short nanoteeth. The diameter of the comb ribbons ranges from 500 to 800 nm, and their lengths are in the range of 2–50 μm. These teeth have a length of

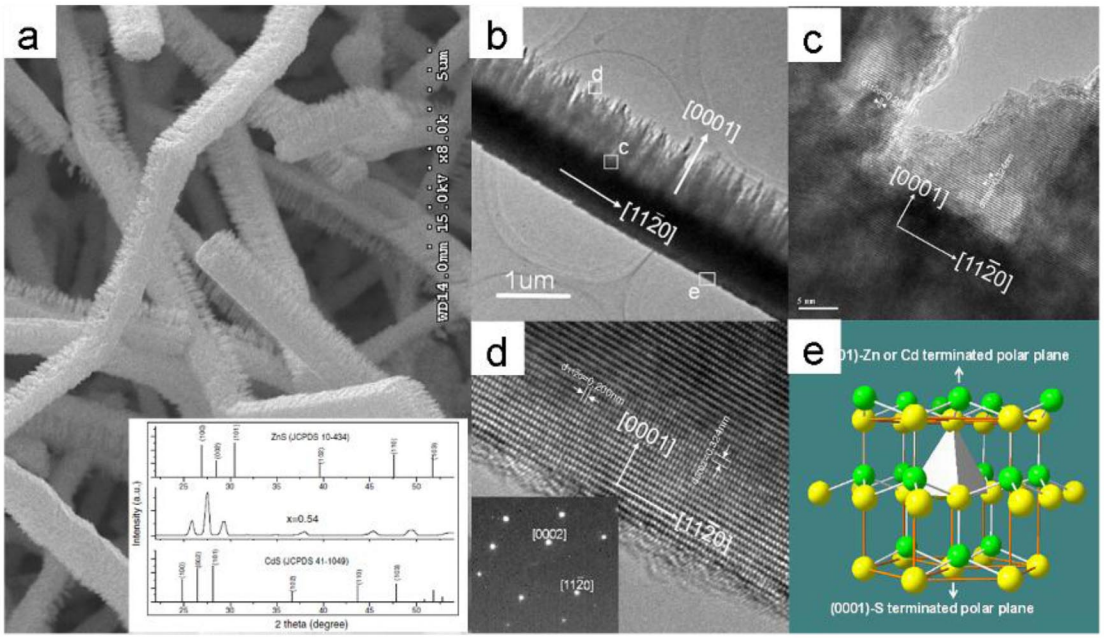

Fig. 22 (a) SEM image and XRD pattern of $Zn_xCd_{1-x}S$ nanocombs; (b) TEM image of a single $Zn_xCd_{1-x}S$ nanocomb; (c, d) HR-TEM images recorded in different regions of the comb; (e) Structure model of wurtzite $Zn_xCd_{1-x}S$. Reproduced from *Chem. Phys. Lett.* **427**, 371 (2006). Copyright © 2006, Elsevier [90].

300–800 nm and a width of 30–100 nm. Additional structure characterization was carried out by using TEM. A low-magnification image of a comb structure is given in Fig. 22b, which clearly displays the one-side teeth structure of the combs. The front-end of the comb teeth shows no catalytic particles, suggesting that the VS mechanism is dominant during the growth process. Figures 22c,d display the HR-TEM images taken in different areas along this array, confirming the monolithically single-crystal nature of the entire comb structure. These also indicate that the comb ribbon grows along the [11–20] directions and the nanoteeth extend along the [0001] directions. The EDS result indicates that the ribbons and teeth have almost the same compositions, with the atomic ratios (Zn+Cd)/S close to 1. The formation of the nanocombs is likely involving a two-step growth process: the first one is the fast growth based on the VS mechanism and along the [11–20] orientation; this results in the formation of the ribbon of the comb; the second one is the subsequent growth of the teeth along the [0001] direction facilitated by a self-catalyzed process, which can be understood from the structure characteristics peculiar to the wurtzite family. The formation of one-sided asymmetric nanocombs can be attributed to the self-catalysis effect of the polar surface. The wurtzite crystal structure has ±(0001) polar surfaces: the (0001) surface is terminated with positively charged Zn or Cd ions and the (000-1) surface is terminated with negatively charged S anions, as marked in Fig. 22e. Thus, both positively charged (0001)-Zn or Cd and negatively charged (000-1)-S polar surfaces can be expected. The positively charged Zn or Cd (0001) surface is chemically active and the negatively charged S (000-1) is relatively inert, resulting in the formation of the comb-teeth along the [0001] orientation as a result of the asymmetric growth [90].

$Zn_xCd_{1-x}S$ zigzag nanowires [92]

While increasing the relative content of $Zn(S_2CNEt_2)_2$ in the mixed $Zn(S_2CNEt_2)_2$ and $Cd(S_2CNEt_2)_2$ precursors, $Zn_xCd_{1-x}S$ single-crystal zigzag nanowires can be fabricated. These nanowires have lengths of up to tens of micrometers and a uniform morphology. The SEM image (Fig. 23a) shows that typical

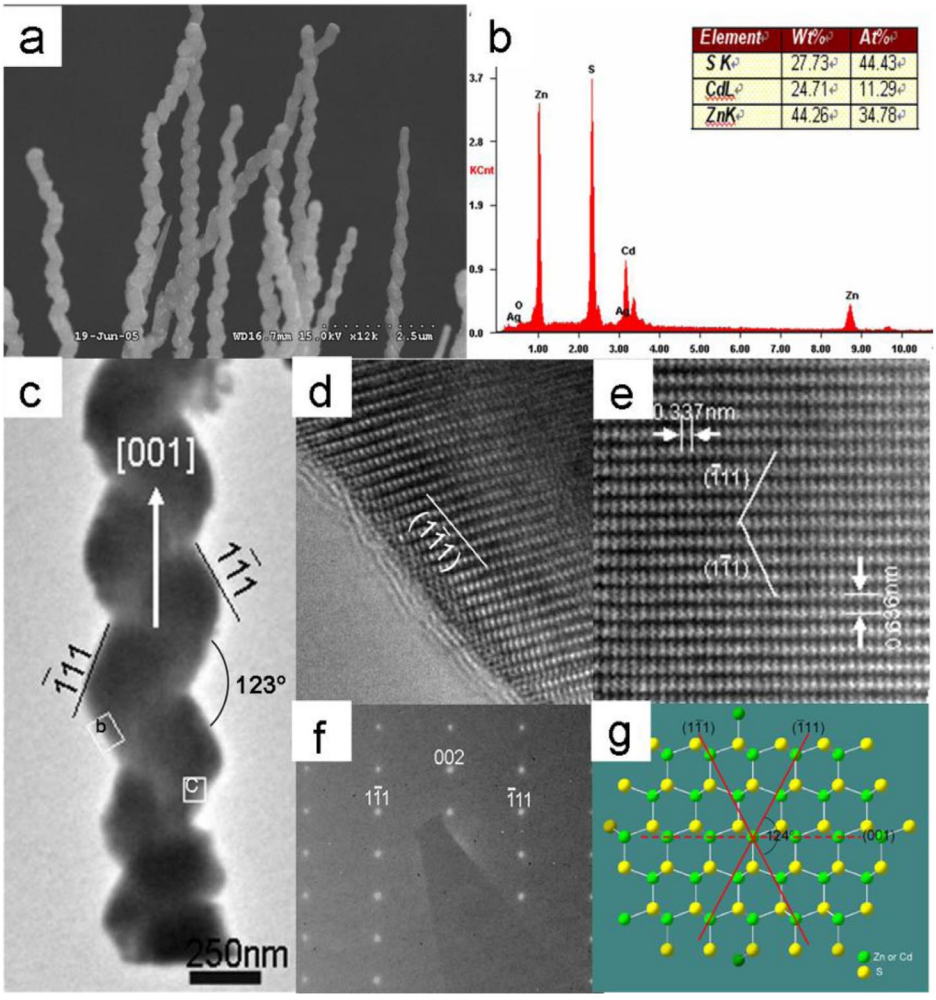

Fig. 23 (a) SEM image and (b) EDS spectrum of $Zn_xCd_{1-x}S$ zigzag nanowires; (c) TEM image and (f) corresponding SAED pattern of a single zigzag nanowire; (d, e) HR-TEM images recorded in different regions of the nanowire; (g) Atomic structure of wurtzite $Zn_xCd_{1-x}S$ projected along the [110] orientation, showing the (001), (1–11), and (–111) planes. Reproduced from *Nanotechnology* **17**, 4644 (2006). Copyright © 2006, Institute of Physics [92].

zigzag nanowire structure and the widths of the nanowires range from 200 to 300 nm. The EDS results indicate that these nanowires are composed of Zn, Cd, and S with the atomic ratios of ~3.1:1:3.9 (Fig. 23b). From the TEM image in Fig. 23c, it can be seen that the nanowire is composed of periodically changing the growth direction domains (along the length direction) with a period close to 300 nm. These ternary nanowires are chemically uniform and possess a good crystal quality along the growth direction in spite of alloying. The HR-TEM and SAED results demonstrate that the whole nanowires are single-crystalline with the growth axis of [001] and periodically alternating growth direction from $[-1\ 1\ 3a^2/2c^2]$ to $[1\ -1\ 3a^2/2c^2]$. Concerning the formation of zigzag nanowires, we suggest that the shear strains and slight fluctuations in the reactions conditions may be the major factors that make the nanowires change the growth direction [92].

CONCLUSION AND OUTLOOK

In conclusion, this paper briefly reviews the authors' recent efforts with respect to the 1D ZnS, CdS, and $Zn_xCd_{1-x}S$ nanostructure syntheses using vapor-phase techniques. Five cases of 1D ZnS nanostructures, three cases of 1D CdS nanostructures, and two cases of 1D $Zn_xCd_{1-x}S$ nanostructures are discussed in detail. Future fascinating achievements toward their applications should inspire more research efforts to address the fundamental and technological challenges that remain. Needless to say, due to the tremendous research efforts and the space limitations, this article is unable to cover all the exciting works reported in this field.

The investigation of these 1D ZnS and CdS nanostructures will be continuously exciting and highly rewarding. Undoubtedly, there will be many innovations and developments on the route toward their practical integration into nanotechnology and many issues need to be solved before that.

(1) Significant challenges still exist to develop simple, efficient, and inexpensive technology to synthesize 1D ZnS and CdS nanostructures; the remaining issues include but are not limited to: reliable control of diameter, length, orientation, density, crystallization, and hierarchical assembly.
(2) Doping of these nanostructures has become an important issue for widening the range of possible applications, in fact, the structure electrical, optical, and magnetic properties can be modified by doping.
(3) Functional nanodevices, such as field-effect transistors, nanolasers, logic gates, nanosensors, and biological systems, need to be developed to meet the rapid miniaturization of electronics down to the nanometer scale.

ACKNOWLEDGMENTS

The authors acknowledge the final support from the Japan Society for the Promotion of Science (JSPS), in the form of a fellowship tenable at the National Institute for Materials Science (NIMS), Tsukuba, Japan (T. Y. Zhai). This work was supported by the International Center for Materials Nanoarchitectonics (MANA) of the National Institute for Materials Science (NIMS), MEXT, Japan.

REFERENCES

1. C. M. Lieber, Z. L. Wang. *MRS Bull.* **32**, 99 (2007).
2. T. Y. Zhai, H. Z. Zhong, Z. J. Gu, A. D. Peng, H. B. Fu, Y. Ma, Y. Y. Li, J. N. Yao. *J. Phys. Chem. C* **111**, 2980 (2007).
3. T. Y. Zhai, Z. J. Gu, Y. Dong, H. Z. Zhong, Y. Ma, H. B. Fu, Y. Y. Li, J. N. Yao. *J. Phys. Chem. C* **111**, 11604 (2007).
4. T. Y. Zhai, X. S. Fang, M. Y. Liao, X. J. Xu, H. B. Zeng, Y. Bando, D. Golberg. *Sensors* **9**, 6504 (2009).
5. Y. N. Xia, P. D. Yang, Y. G. Sun, Y. Y. Wu, B. Mayers, B. Gates, Y. D. Yin, F. Kim, H. Q. Yan. *Adv. Mater.* **15**, 353 (2003).
6. X. J. Xu, G. T. Fei, W. H. Yu, X. W. Wang, L. Chen, L. D. Zhang. *Nanotechnology* **17**, 426 (2006).
7. G. Z. Shen, J. H. Cho, J. K. Yoo, G. C. Yi, C. J. Lee. *J. Phys. Chem. B* **109**, 9294 (2005).
8. Z. L. Wang. *ACS Nano* **2**, 1987 (2008).
9. Z. L. Wang. *Mater. Sci. Eng. R* **64**, 33 (2009).
10. X. S. Fang, Y. Bando, U. K. Gautam, T. Y. Zhai, H. B. Zeng, X. J. Xu, M. Y. Liao, D. Golberg. *Crit. Rev. Mater. Sci.* **34**, 190 (2009).
11. X. S. Fang, Y. Bando, D. Golberg. *J. Mater. Sci. Technol.* **24**, 512 (2008).
12. D. Moore, Z. L. Wang. *J. Mater. Chem.* **16**, 3898 (2006).
13. X. S. Fang, L. D. Zhang. *J. Mater. Sci. Technol.* **22**, 721 (2006).
14. P. D. Yang, Y. Y. Wu, R. Fan. *Int. J. Nanosci.* **1**, 1 (2002).

15. Z. J. Gu, Y. Ma, T. Y. Zhai, B. F. Gao, W. S. Yang, J. N. Yao. *Chem.—Eur. J.* **12**, 7717 (2006).
16. Z. J. Gu, T. Y. Zhai, B. F. Gao, G. J. Zhang, D. M. Ke, Y. Ma, J. N. Yao. *Cryst. Growth Des.* **7**, 825 (2007).
17. Z. J. Gu, T. Y. Zhai, B. F. Gao, X. H. Sheng, Y. B. Wang, H. B. Fu, Y. Ma, J. N. Yao. *J. Phys. Chem. B* **110**, 23829 (2006).
18. X. Wang, H. B. Fu, A. D. Peng, T. Y. Zhai, Y. Ma, F. L. Yuan, J. N. Yao. *Adv. Mater.* **21**, 1636 (2009).
19. L. Y. Zhao, W. S. Yang, Y. Luo, T. Y. Zhai, G. J. Zhang, J. N. Yao. *Chem.—Eur. J.* **11**, 3773 (2005).
20. L. Y. Zhao, W. S. Yang, G. J. Zhang, T. Y. Zhai, J. N. Yao. *Chem. Phys. Lett.* **379**, 479 (2003).
21. M. Chang, X. L. Cao, X. J. Xu, L. D. Zhang. *Phys. Lett. A* **372**, 273 (2008).
22. J. D. Holmes, K. P. Johnston, R. C. Doty, B. A. Korgel. *Science* **287**, 1471 (2000).
23. N. I. Kovtyukhova, T. E. Mallouk, T. S. Mayer. *Adv. Mater.* **15**, 780 (2003).
24. B. A. Korgel, D. Fitzmautice. *Adv. Mater.* **10**, 661 (1998).
25. D. Li, Y. Wang, Y. Xia. *Adv. Mater.* **16**, 361 (2004).
26. Y. Zhao, X. Y. Cao, L. Jiang. *J. Am. Chem. Soc.* **129**, 764 (2007).
27. Y. W. Jun, J. S. Choi, J. Cheon. *Angew. Chem., Int. Ed.* **45**, 3414 (2006).
28. A. R. Tao, S. Habas, P. D. Yang. *Small* **4**, 310 (2008).
29. Y. N. Xia, Y. J. Xiong, B. Lim, S. E. Skrabalak. *Angew. Chem., Int. Ed.* **48**, 60 (2009).
30. G. Z. Shen, D. Chen, Y. Bando, D. Golberg. *J. Mater. Sci. Technol.* **24**, 541 (2008).
31. C. J. Barrelet, Y. Wu, D. C. Bell, C. M. Lieber. *J. Am. Chem. Soc.* **125**, 11498 (2003).
32. Y. W. Wang, L. D. Zhang, C. H. Liang, G. Z. Wang, X. S. Peng. *Chem. Phys. Lett.* **357**, 314 (2002).
33. S. Kar, S. Chaudhuri. *J. Phys. Chem. B* **109**, 3298 (2005).
34. X. C. Jiang, Y. Xie, J. Lu, L. Y. Zhu, W. He, Y. T. Qian. *Chem. Mater.* **13**, 1213 (2001).
35. Y. Jiang, X. M. Meng, J. Liu, Z. R. Hong, C. S. Lee, S. T. Lee. *Adv. Mater.* **15**, 1195 (2003).
36. Q. H. Xiong, G. Chen, J. D. Acord, X. Liu, J. J. Zengel, H. R. Gutierrez, J. M. Redwing, L. C. Lew Yan Voon, B. Lassen, P. C. Eklund. *Nano Lett.* **4**, 1663 (2004).
37. J. X. Ding, J. A. Zapien, W. W. Chen, Y. Lifshitz, S. T. Lee. *Appl. Phys. Lett.* **85**, 2361 (2004).
38. X. M. Meng, J. Liu, Y. Jiang, W. W. Chen, C. S. Lee, I. Bello. S. T. Lee. *Chem. Phys. Lett.* **382**, 434 (2003).
39. L. W. Yin, Y. Bando, J. H. Zhan, M. S. Li, D. Golberg. *Adv. Mater.* **17**, 1972 (2005).
40. L. Dloczik, R. Engelhardt, K. Ernst, S. Fiechter, I. Sieber, R. Könenkamp. *Appl. Phys. Lett.* **78**, 3687 (2001).
41. Y. C. Zhu, Y. Bando, Y. Uemura, *Chem. Commun.* 836 (2003).
42. H. Zhang, S. Y. Zhang, S. Pan, G. P. Li, J. G. Hou. *Nanotechnology* **15**, 945 (2004).
43. T. Y. Zhai, Z. J. Gu, Y. Ma, W. S. Yang, L. Y. Zhao, J. N. Yao. *Mater. Chem. Phys.* **100**, 281 (2006).
44. X. S. Fang, Y. Bando, C. H. Ye, D. Golberg. *Chem. Commun.* 3048 (2007).
45. X. S. Fang, Y. Bando, M. Y. Liao, U. K. Gautam, C. Y. Zhi, B. Dierre, B. D. Liu, T. Y. Zhai, T. Sekiguchi, Y. Koide, D. Golberg. *Adv. Mater.* **21**, 2034 (2009).
46. C. Ma, D. Moore, J. Li, Z. L. Wang. *Adv. Mater.* **15**, 228 (2003).
47. Y. Jiang, X. M. Meng, J. Liu, Z. Y. Xie, C. S. Lee, S. T. Lee. *Adv. Mater.* **15**, 323 (2003).
48. X. D. Li, X. N. Wang, Q. H. Xiong, P. C. Eklund. *Nano Lett.* **5**, 1982 (2005).
49. Z. X. Zhang, J. X. Wang, H. J. Yuan, Y. Gao, D. F. Liu, L. Song, Y. J. Xiang, X. W. Zhao, L. F. Liu, S. D. Luo, X. Y. Dou, S. C. Mou, W. Y. Zhou, S. S. Xie. *J. Phys. Chem. C* **109**, 18352 (2005).
50. G. Z. Shen, Y. Bando, J. Q. Hu, D. Golberg. *Appl. Phys. Lett.* **90**, 123101 (2007).
51. J. F. Gong, S. G. Yang, H. B. Huang, J. H. Duan, H. W. Liu, X. N. Zhao, R. Zhang, Y. W. Du. *Small* **2**, 732 (2006).

52. T. Y. Zhai, Y. Dong, Y. B. Wang, Z. W. Cao, Y. Ma, H. B. Fu, J. N. Yao. *J. Solid State Chem.* **181**, 950 (2008).
53. T. Y. Zhai, Z. J. Gu, H. B. Fu, Y. Ma, J. N. Yao. *Cryst. Growth Des.* **7**, 1388 (2007).
54. X. S. Fang, Y. Bando, G. Z. Shen, C. H. Ye, U. K. Gautam, P. M. F. J. Costa, C. Y. Zhi, C. C. Tang, D. Golberg. *Adv. Mater.* **19**, 2593 (2007).
55. X. S. Fang, Y. Bando, U. K. Gautam, C. H. Ye, D. Golberg. *J. Mater. Chem.* **18**, 509 (2008).
56. X. S. Fang, U. K. Gautam, Y. Bando, B. Dierre, T. Sekiguchi, D. Golberg. *J. Phys. Chem. C* **112**, 4735 (2008).
57. S. Biswas, T. Ghoshal, S. Kar, S. Chakrabarti, S. Chaudhuri. *Cryst. Growth Des.* **8**, 2171 (2008).
58. Y. Q. Chang, M. W. Wang, X. H. Chen, S. L. Ni, Q. J. Qiang. *Solid State Commun.* **142**, 295 (2007).
59. P. K. Ghosh, U. N. Maiti, S. Jana, K. K. Chattopadhyay. *Appl. Surf. Sci.* **253**, 1544 (2006).
60. Z. G. Chen, J. Zou, G. Liu, X. D. Yao, F. Li, X. L. Yuan, T. Sekiguchi, G. Q. Li, H. M. Cheng. *Adv. Funct. Mater.* **18**, 3063 (2008).
61. X. F. Duan, C. M. Lieber. *Adv. Mater.* **12**, 298 (2000).
62. D. Routkevitch, T. Bigioni, M. Moskovits, J. M. Xu. *J. Phys. Chem.* **100**, 14037 (1996).
63. C. B. Mao, D. J. Solis, B. D. Reiss, S. T. Kottmann, R. Y. Sweeney, A. Hayhurst, G. Georgiou, B. Iverson, A. M. Becher. *Science* **303**, 213 (2004).
64. C. H. Ye, G. W. Meng, Y. H. Wang, Z. Jiang, L. D. Zhang. *J. Phys. Chem. B* **106**, 10338 (2002).
65. J. P. Ge, Y. D. Li. *Adv. Funct. Mater.* **14**, 157 (2004).
66. H. Zhang, X. Y. Ma, J. Xu, J. J. Niu, J. Sha, D. R. Yang. *J. Cryst. Growth* **246**, 108 (2002).
67. D. S. Xu, Y. J. Xu, D. P. Chen, G. L. Guo, L. L. Gui, Y. Q. Tang. *Adv. Mater.* **12**, 520 (2000).
68. Y. J. Xiong, Y. Xie, J. Yang, R. Zhang, C. Z. Wu, G. A. Du. *J. Mater. Chem.* **12**, 3712 (2002).
69. X. P. Shen, A. H. Yuan, F. Wang, J. M. Hong, Z. Xu. *Solid State Commun.* **133**, 19 (2005).
70. H. Zhang, X. Y. Ma, J. Xu, D. R. Yang. *J. Cryst. Growth* **263**, 372 (2004).
71. M. W. Shao, F. Xu, Y. Y. Peng, J. Wu, Q. Li, S. Y. Zhang, Y. T. Qian. *New J. Chem.* **26**, 1440 (2002).
72. X. M. Li, H. B. Chu, Y. Li. *J. Solid State Chem.* **179**, 96 (2006).
73. L. F. Dong, J. Jiao, M. Coulter, L. Love. *Chem. Phys. Lett.* **376**, 653 (2003).
74. T. Gao, T. H. Wang. *J. Phys. Chem. B* **108**, 20045 (2004).
75. Y. K. Liu, J. A. Zapien, C. Y. Geng, Y. Y. Shan, C. S. Lee, Y. Lifshitz, S. T. Lee. *Appl. Phys. Lett.* **85**, 3241 (2004).
76. J. Zhang, F. H. Jiang, L. D. Zhang. *J. Phys. Chem. B* **108**, 7002 (2004).
77. Z. Q. Wang, J. F. Gong, J. H. Duan, H. B. Huang, S. G. Yang, X. N. Zhao, R. Zhang, Y. W. Du. *Appl. Phys. Lett.* **89**, 033102 (2006).
78. K. Y. Lee, J. R. Lim, H. Pho, Y. J. Choi, K. J. Choi, J. G. Park. *Appl. Phys. Lett.* **91**, 201901 (2007).
79. P. V. Radovanovic, C. J. Barrelet, S. Gradečak, F. Qian, C. M. Lieber. *Nano Lett.* **5**, 1407 (2005).
80. T. Y. Zhai, Z. J. Gu, H. Z. Zhong, Y. Dong, Y. Ma, H. B. Hu, Y. F. Li, J. N. Yao. *Cryst. Growth Des.* **7**, 488 (2007).
81. T. Y. Zhai, X. S. Fang, Y. Bando, Q. Liao, X. J. Xu, H. B. Zeng, Y. Ma, J. N. Yao, D. Golberg. *ACS Nano* **3**, 949 (2009).
82. T. Y. Zhai, X. S. Fang, Y. Bando, B. Dierre, B. D. Liu, H. B. Zeng, X. J. Xu, Y. Huang, X. L. Yuan, T. Sekiguchi, D. Golberg. *Adv. Funct. Mater.* **19**, 2423 (2009).
83. G. X. Qian, K. F. Huo, J. J. Fu, T. F. Hung, P. K. Chu. *J. Appl. Phys.* **104**, 014312 (2008).
84. Q. Tang, X. H. Chen, T. Li, Z. W. Zhao, Y. T. Qian, D. P. Yu, W. C. Yu. *Chem. Lett.* **33**, 1088 (2004).
85. H. Y. Li, J. M. Green, J. Jiao. *J. Phys. Chem. C* **112**, 15140 (2008).
86. Y. F. Lin, Y. J. Hus, S. Y. Lu, S. C. Kung. *Chem. Commun.* 2391 (2006).
87. Y. F. Lin, Y. J. Hsu, S. Y. Lu, K. T. Chen, T. Y. Tseng. *J. Phys. Chem. C* **111**, 13418 (2007).

88. Y. K. Liu, J. A. Zapien, Y. Y. Shan, C. Y. Geng, C. S. Lee, S. T. Lee. *Adv. Mater.* **17**, 1372 (2005).
89. A. L. Pan, H. Yang, R. B. Liu, R. C. Yu, B. S. Zou, Z. L. Wang. *J. Am. Chem. Soc.* **127**, 15692 (2005).
90. T. Y. Zhai, X. Z. Zhang, W. S. Yang, Y. Ma, J. F. Wang, Z. J. Gu, D. P. Yu, H. Yang, J. N. Yao. *Chem. Phys. Lett.* **427**, 371 (2006).
91. X. Z. Zhang, T. Y. Zhai, Y. Ma, J. N. Yao, D. P. Yu. *J. Electron Microsc.* **57**, 7 (2008).
92. T. Y. Zhai, Z. J. Gu, W. S. Yang, X. Z. Zhang, J. Huang, Y. S. Zhao, D. P. Yu, H. B. Fu, Y. Ma, J. N. Yao. *Nanotechnology* **17**, 4644 (2006).

